remote sensing

MDPI

Article

A Unified Formulation for the Computation of the Six-Degrees-of-Freedom-Motion-Induced Errors in Floating Doppler Wind LiDARs

Andreu Salcedo-Bosch [1], Joan Farré-Guarné [1], Marcos Paulo Araújo da Silva [1] and Francesc Rocadenbosch [1,2,*]

[1] CommSensLab, Department of Signal Theory and Communications, Universitat Politècnica de Catalunya (UPC), E-08034 Barcelona, Spain
[2] Institut d'Estudis Espacials de Catalunya (IEEC), Universitat Politècnica de Catalunya, E-08034 Barcelona, Spain
* Correspondence: francesc.rocadenbosch@upc.edu

Abstract: This work presents an analytical formulation to assess the six-degrees-of-freedom-motion-induced error in floating Doppler wind LiDARs (FDWLs). The error products derive from the horizontal wind speed bias and apparent turbulence intensity. Departing from a geometrical formulation of the FDWL attitude and of the LiDAR retrieval algorithm, the contributions of the rotational and translational motion to the FDWL-measured total error are computed. Central to this process is the interpretation of the velocity–azimuth display retrieval algorithm in terms of a first-order Fourier series. The obtained 6 DoF formulation is validated numerically by means of a floating LiDAR motion simulator and experimentally in nearshore and open-sea scenarios in the framework of the Pont del Petroli and IJmuiden campaigns, respectively. Both measurement campaigns involved a fixed and a floating *ZephIR*^{TM} 300 LiDAR. The proposed formulation proved capable of estimating the motion-induced FDWL horizontal wind speed bias and returned similar percentiles when comparing the FDWL with the fixed LiDAR. The estimations of the turbulence intensity increment statistically matched the FDWL measurements under all motional and wind scenarios when clustering the data as a function of the buoy's mean tilt amplitude, mean translational-velocity amplitude, and mean horizontal wind speed.

Keywords: Doppler wind LiDAR; floating LiDAR system; turbulence intensity; motion-induced error; six degrees of freedom; wind energy

Citation: Salcedo-Bosch, A.; Farré-Guarné, J.; Araújo da Silva, M.P.; Rocadenbosch, F. A Unified Formulation for the Computation of the Six-Degrees-of-Freedom-Motion-Induced Errors in Floating Doppler Wind LiDARs. *Remote Sens.* **2023**, *15*, 1478. https://doi.org/10.3390/rs15061478

Academic Editor: Sergei Badulin

Received: 3 February 2023
Revised: 3 March 2023
Accepted: 4 March 2023
Published: 7 March 2023

1. Introduction

The more homogeneous and stronger wind fields found on open-sea environments make offshore wind energy a dependable source of electricity generation [1,2]. In the last few decades, the wind energy industry has made important investments in offshore wind energy [3]. Specifically, a cumulative offshore wind capacity of 35 GW was deployed around the world in 2020, with Europe and China standing out in the market [4]. However, it is still one of the most expensive sources of renewable energy [5], and cost reduction is the main goal of the industry [6,7]. One of the main considerations is to obtain reliable data to assess the viability of a future wind farm based on the location. Usually, offshore wind farms are deployed in shallow waters, but there is a tendency to go further offshore and to deeper waters [8], where a higher wind capacity can be obtained. At those locations, the traditional technology used for atmospheric assessment, namely meteorological masts planted on the seabed, is no longer an option. This motivates the use of alternative remote sensing sensors such as satellites [9,10], radars [11], sodars [12,13], and combined methods [14,15]. Nevertheless, due to the high requirements of the industry in terms of the measurement

accuracy, temporal and spatial resolution, and data availability, Doppler Wind LiDARs (DWLs) have become the most trusted devices for wind remote sensing [7].

In general, two types of DWLs are used for wind remote sensing: *pulsed* and *focusable continuous-wave* (CW) DWLs [16]. Pulsed DWLs use the time of flight to build up a vertically resolved wind profile, whereas focusable CW DWLs achieve the same by focusing the emitted beam on a particular height by changing its optics. Among pulsed DWLs, two main detection techniques are used: direct detection and heterodyne detection. Direct detection utilizes an optical frequency analyzer, typically an interferometer, and the receiver directly measures the signal photoelectrons [17], whereas in heterodyne detection, the backscattered signal is mixed with the frequency-offset version of the beam of a local oscillator laser, and the receiver measures the resultant beating frequency [18].

When placed over floating platforms or buoys, DWLs are able to measure the wind profile in a cost-effective way [7,19,20]. Moreover, in contrast to metmasts, they can easily be redeployed and thus cover large areas [21]. On the other hand, FDWLs suffer 6 degrees of freedom (DoF) motion, induced by the waves [22–24], which increases the variance on the reconstructed wind vector by the LiDAR [25,26]. However, in wind energy standard averaging periods, typically 10 or 30 min, the motion-induced error on the retrieved mean wind vector can be neglected, as it is averaged out [25,27–29].

The motion-induced variance in FDWL measurements is encountered at higher wind statistical moments, such as the turbulence intensity (TI) [28]. The TI is defined as the ratio between the standard deviation of the horizontal wind speed (HWS) and the mean HWS. In the presence of the wave motion, FDWLs measure an apparent added turbulence due to the motion-induced variance, which corrupts the TI measurements [25,26]. TI is one of the parameters of main importance for wind farm design and operation, as wrong estimates of TI could lead to turbine overdesign or malfunctioning [30] and thus higher costs.

In the state of the art, the study of the motion-induced error on FDWLs is twofold: error estimation and error compensation. This paper addresses the former topic, specifically, error estimation in focusable CW FDWLs, which is carried out using a thorough analytical formulation of the system mechanics and the wind vector retrieval algorithm. The error estimation in pulsed FDWLs has been addressed elsewhere [31,32]. The latter topic, i.e., error compensation, using either mechanical [27] or signal processing techniques [25,28,33,34] is outside the scope of the present work.

So far, multiple studies have addressed the study of the motion-induced *error* on focusable CW FDWLs on both the scan-time and 10 min levels:

On the scan-time level, Tiana-Alsina et al. [35] proposed a basic CW FDWL motion simulator, in which the roll and pitch motions were simulated by means of Euler's rotation matrices. This simulator provided insights on the HWS error in relation to the wind direction (WD) and the buoy tilt but was unable to simulate the effects of the translational motion on the HWS error. Bischoff et al. [36] presented a simulation environment to estimate the uncertainties in the measurements by CW FDWLs using a simplified buoy model. However, the error estimates could not match the measurements for the high-resolution (1 Hz) data. Kelberlau et al. [28] provided a thorough geometrical description of the FDWL dynamics taking into account the 6 DoF motion of the FDWL buoy and provided a method for compensating the apparent TI measured by the SEAWATCH CW FDWL buoy by Fugro^{TM}. This geometrical description permitted a preliminary study of the 6-DoF-motion-induced error in a LiDAR scan but was limited by the oversimplification of assuming a constant value for the initial scan phase. Departing from this geometrical description, Salcedo et al. numerically simulated the 6 DoF CW DWL measurement error [37] and provided a first 6 DoF motion correction algorithm using an unscented Kalman filter [33]. The simulator [37] modeled each of the six DoF as a sinusoidal signal with a given amplitude, frequency, and phase and enabled full understanding of the motion-induced error in a LiDAR scan through the principle of error superposition. Most of the CW FDWL motion-related error studies in the literature resorted to numerical simulations due to the inherent complexity of the velocity–azimuth display (VAD) algorithm, because it

involves a least squares fit as a nonlinear operation. These simulations are computationally expensive and difficult to implement [35–38].

On the 10 min level, Kelberlau et al. [38] recently presented a study on the motion-induced error in the measurement of the mean HWS using a motion simulator. The study theoretically proved the reduced sensitivity of the mean HWS error to the LiDAR motion and its relation to the buoy motion frequency. However, the study was limited to the mean HWS and provided error values up to one order of magnitude smaller than the typically measured values. The study by Bischoff et al. [36] was also limited to studying the bias in the HWS mean, and difficulties in validating the estimated values with the experimental data were encountered. Gutiérrez-Antuñano et al. [25] presented a method to estimate the TI measurement error based on a 2 DoF (roll and pitch) motion simulator as a way to compensate for this error. Overall, it showed good estimation of the motion-induced error, but the performance of the method largely depended on the motion scenario because only two DoF were taken into account. In addition, the simulation was computationally demanding.

The above considerations motivate the study of a unified 6 DoF (rotational and translational) method to quantify the motion-induced error in focusable CW FDWLs: In this work, we provide, for the first time, a complete *analytical formulation* and calculus of the 6-DoF-motion-induced error on the HWS retrieved by the focusable CW FDWL in a scan. The formulation relies on the VAD LiDAR wind retrieval algorithm and motion parameterization using the characteristic amplitude, frequency, and phase of each of the six DoF (i.e., three rotational and three translational components). Methods to statistically quantify the 10 min HWS bias and the TI increment in response to the floating LiDAR motion are also derived. The framework is the focusable continuous-wave $ZephIR^{TM}$ 300 LiDAR, using experimental data gathered during the "Pont del Petroli" and IJmuiden measurement campaigns.

This paper is structured as follows: Section 2 presents the "Pont del Petroli" and IJmuiden measurement campaigns and describes the instrumentation used; Section 3 describes the analytical motion model of the FDWL and presents the motion estimation method; Section 4 validates the analytical model by means of the simulation [37] and the experimental measurements from the "Pont del Petroli" and IJmuiden campaigns; Section 5 gives some concluding remarks.

2. Materials

2.1. Pont del Petroli Campaign

The Pont-del-Petroli (PdP) campaign took place in June 2013 at the "Pont del Petroli" pier (Badalona, Barcelona, Spain) [39]. It aimed to assess the wind measurement capabilities of a proof-of-concept FDWL buoy in the context of the NEPTUNE project by comparing its performance against a fixed LiDAR [27]. Both the fixed and the FDWL were ZephIR 300 focusable continuous-wave DWLs. The fixed LiDAR was situated at the PdP pier in a standstill configuration. The FDWL was deployed offshore 50 m away from the fixed LiDAR. Both ZephIR 300s were identical instruments and were calibrated onshore one beside the other for a period of 3 h. They were configured to measure the wind at a height of 100 m above sea level (a.s.l.), and the calibration ensured identical measurements at 1 s and 10 min intervals. The experiment surroundings were dominated by an open-sea topology in the south and east directions and an urban topology in the west and north directions. The coastline followed the southwestern to northeastern direction.

ZephIR 300 DWL. The ZephIR 300 is a continuous-wave focusable Doppler LiDAR specially conceived for offshore operation [40]. It is able to measure the wind at user-defined heights from 10 m up to 200 m in steps of 1 m [41]. In order to retrieve the wind vector for a particular measurement height, the ZephIR 300 measures the Doppler radial speed along 50 lines of sight (LoSs) every second over a scanning cone of a 30 deg aperture from the zenith. A wedge prism rotating with a uniform circular motion of one revolution per second is used to steer the laser beam in the directions of the 50 LoSs. In uniform wind,

the projection of the wind vector along the 50 LoSs, as a function of the azimuth scanning angle (i.e., the so called *VAD function*), takes the shape of a cosine. The LiDAR uses the VAD algorithm to retrieve the wind vector from the LoSs by fitting a cosine function to the LoS measurements [16]. The ZephIR 300 is a homodyne detection LiDAR, which means that it cannot discern the sign of the Doppler shift. As a result, the VAD function takes the form of a rectified cosine wave, creating an ambiguity of $\pm$180 deg for the WD measurement [42]. The ZephIR 300 is equipped with a wind vane to disambiguate the WD.

FDWL buoy. The FDWL buoy is a proof-of-concept experimental buoy specially conceived to host a ZephIR 300 LiDAR in an offshore operation [43,44]. It weighs 3 tons and has a width of 3.77 m. It consists of a four-floater structure designed to conform with the wind energy measurement requirements as well as to monitor multiple sea-related parameters. Apart from the ZephIR 300, it hosts a MicroStrain 3DM-GX3-45 inertial measurement unit (IMU) that was used to monitor the 6 DoF motion of the lidar.

3DM-GX3-45 IMU. The IMU consists of a GPS unit, an accelerometer, a magnetometer, and a gyro [45], measuring the LiDAR's tilt and velocity at a 10 Hz sampling frequency. The IMU was located on the bottom of the FDWL buoy structure. We defined, at the location of this FDWL buoy bottom, an inertial right-handed clockwise north–east–down (NED) frame of reference. The gyro separately measured the angular accelerations around the north, east, and down axes, and the accelerometer measured the translational accelerations along these axes. In order to avoid incurring an accumulated error when integrating the accelerations, the 3DM-GX3-45 uses an extended Kalman filter, which permits the monitoring of the buoy's attitude by considering the GPS and magnetometer measurements. The 3DM-GX3-45 is able to measure the buoy's velocity and tilt with an accuracy of $\pm$0.1 m/s and $\pm$0.35 deg, respectively.

2.2. IJmuiden Campaign

The IJmuiden campaign took place between 1 April and 1 June 2015 at the IJmuiden metmast test facilities (North Sea, 85 km offshore of the Netherlands coast). The goal of the campaign was to validate the precommercial FDWL buoy EOLOS^{TM} against the reference IJmuiden metmast, located 300 m apart. The EOLOS^{TM} FDWL was similar to the FDWL used in the PdP campaign but prepared for harsher scenarios and higher endurance. The FDWL buoy hosted a ZephIR^{TM} 300 DWL and a 3DM-GX3-45 IMU as well. The FDWL was configured to sense the wind profile at four different heights (25, 38, 56, and 83 m) coincidental with the measurement heights of the metmast anemometers. An identical ZephIR^{TM} 300 DWL was installed on the metmast platform (21 m) sensing the wind above the metmast top from 90 m up to 315 m every 25 m.

3. Methods

3.1. Basic Definitions

The instantaneous wind vector $\vec{u}$ ($\vec{u} = \vec{U} + \vec{u'}$, where $\vec{U}$ denotes the mean wind and $\vec{u'}$ the turbulent component) is defined as the three-dimensional vector (u_1, u_2, u_3) computed here from the HWS, WD, and vertical wind speed (VWS) as

$$\vec{u} = [HWS \cdot \cos(WD), HWS \cdot \sin(WD), VWS]. \quad (1)$$

In wind energy, the 10 min mean wind vector is the usual standard, and hereafter, HWS , WD, and VWS refer to the *10 min mean values* unless otherwise indicated.

The TI is indicative of the HWS variations with respect to the mean HWS, and it is computed as

$$TI = \frac{\sigma_{HWS}}{HWS}, \quad (2)$$

where σ_{HWS} is the 10 min HWS standard deviation.

Instantaneous error. To study the motion-induced FDWL measurement error in the retrieved HWS at the *i-th lidar scan*, we defined the "instantaneous" error (in practice, the 1 s error considering a scan rate of 1 scan/s) as

$$\epsilon_{HWS,i} = \hat{HWS}_i - HWS_i, \tag{3}$$

where $\hat{HWS}$ denotes the HWS "estimated" by the VAD algorithm, and HWS_i denotes the "true" HWS at the *i-th* scan.

10 min error. The wind energy industry is interested in quantifying both the HWS measurement bias and the TI increment due to the wave-induced motion on FDWLs at a 10 min level.

The *bias* during a sequence of N measurement scans (i.e., the sample statistical interval; usually $N = 600$ for 10 min measurements when measuring at a single height) is defined as the difference between the mean HWS measured by the FDWL and the mean HWS measured by the reference fixed LiDAR. Formally,

$$bias_{meas} = \frac{1}{N}\sum_{i=1}^{N} \hat{HWS}_i - \frac{1}{N}\sum_{i=1}^{N} HWS_i = \frac{1}{N}\sum_{i=1}^{N} \epsilon_{HWS,i}. \tag{4}$$

Statistically, it can be expressed as

$$bias_{est} = E[\hat{HWS}] - HWS = E[\epsilon_{HWS,i}], \tag{5}$$

where $E[\cdot]$ denotes the expectation operator, $\hat{HWS}$ is the 10 min horizontal wind speed estimated by the FDWL, and HWS is the "true" 10 min horizontal wind speed.

The TI increment, ΔTI_{meas}, is defined as the TI measured by the FDWL minus the TI measured by the reference fixed LiDAR. Formally,

$$\Delta TI_{meas} = \left.\frac{\sigma_{HWS_{FDWL}}}{\overline{HWS}_{FDWL}}\right|_{bin} - \left.\frac{\sigma_{HWS_{fixed}}}{\overline{HWS}_{fixed}}\right|_{bin}, \tag{6}$$

where the *overbar* denotes the "mean" over the 10 min HWS samples in the calculus bin.

On the other hand, the TI increment can be estimated as

$$\Delta TI_{est} = \frac{\sigma_{\epsilon_{HWS,i}}}{HWS}, \tag{7}$$

where $\sigma_{\epsilon_{HWS,i}}$ is the standard deviation of the instantaneous error (Equation (3)).

3.2. Reconciling the Estimated and the Measured TI

Next, we related Equation (7) to Equation (6) from a statistical and probabilistic theoretical perspective. Toward this goal and in order to aid the mathematical notation, we introduce the *short-hand notation* F-R-W as follows: we changed the mnemonics "FDWL" into "F" and "fixed" into "R" (representing "reference" fixed LiDAR). We also introduce the subscript "W" to denote the wind that a *nonmoving DWL* would measure *at the same place* as the moving FDWL. In other words, subscript "W" denotes the "true" wind measurement but includes the 1 s average and spatial smoothing inherent to the DWL scanning procedure. To simplify the notation, the "true" wind HWS, HWS_W, is simply denoted as HWS.

3.2.1. On the Estimated TI

According to probability theory, the variance in the difference of two random variables (i.e., $\epsilon_{F,W} = HWS_F - HWS_W$, which reproduces Equation (3)) is equal to the sum of each of their variances minus twice their covariance [46],

$$\sigma^2_{\epsilon_{F,W}} = \sigma^2_F + \sigma^2_W - 2\rho\sigma_F\sigma_W, \tag{8}$$

where ρ is the correlation coefficient between the "F" and "W" variables, and $cov(F, W) = \rho_{F,W}\sigma_F\sigma_W$.

At this point, we introduce the assumption that the FDWL-measured and the "true" HWS (subscripts "F" and "W", respectively) are linearly correlated so that $\rho_{F,W} \approx 1$. By experiment, Tiana-Alsina et al. [35] reported correlation coefficients of $\rho_{F,R} = 0.9$, $\rho_{F,R} = 0.86$, and $\rho_{F,R} = 0.66$ between the co-located moving and reference DWLs in a controlled-motion experiment for tilt motion amplitudes of 10, 16, and 25 deg, respectively. In past experimental campaigns involving different FDWL buoy topologies [23,25,28,38], the most frequent buoy tilts were reported to range from 0 up to 10 deg. These low tilts are also supportive of high F-to-W correlation coefficients, $\rho_{F,W} \approx 1$, at the FDWL location. Inserting $\rho_{F,W} = 1$ in Equation (8) above and rearranging the terms, we obtain

$$\sigma^2_{\epsilon_{F,W}} \simeq (\sigma_F - \sigma_W)^2. \tag{9}$$

By taking the square root of Equation (9) above and substituting it into Equation (7), the estimated turbulence intensity can be written as

$$\Delta TI_{est} \simeq \frac{\sigma_F - \sigma_W}{HWS}. \tag{10}$$

3.2.2. On the Measured TI

As in the preceding subsection, one can assume that the 10 min FDWL- and the reference-LiDAR-measured HWS are virtually identical so that $HWS_{FDWL} \approx HWS_{fixed} \approx HWS$ [20,29]. Introducing this approximation into Equation (6) and using the shorthand notation F-R-W introduced above, it can be rewritten as

$$\Delta TI_{meas} = \frac{\sigma_F - \sigma_R}{HWS}. \tag{11}$$

If the FDWL and the fixed LiDAR carried out exactly co-located measurements, the estimated TI (Equation (10)) and the measured TI (Equation (11)) *would be* identical (i.e., $\sigma_R = \sigma_W$). In practice, the fixed and the FDWL were located 50 m apart in the PdP campaign and 300 m apart in the IJmuiden campaign (see Section 2); therefore, small differences up to 1% [33] were expected to arise between the estimated and the measured TI increment when different wind flows were measured by the reference and floating LiDARs.

3.3. FDWL Geometrical Model

We defined the right-handed Cartesian XYZ "moving body" coordinate system of the LiDAR buoy (hereafter, the "moving" coordinate system) and the right-handed Cartesian north–east–down (NED) "fixed" inertial frame of reference (hereafter, the "fixed" system, Figure 1). The IMU (see Section 2) measured the rotation and translation of the "moving" coordinate system with respect to the "fixed" system. The vectors $\hat{n}$, $\hat{e}$, and $\hat{d}$ were the unitary vectors aligned with the N, E, and D axes of the fixed coordinate system, respectively. $\hat{x}$, $\hat{y}$, and $\hat{z}$ were the unitary vectors aligned with the X, Y, and Z axes, respectively, of the moving coordinate system. $\hat{h}$ was a unit vector in the outbound direction of the LiDAR scanning cone axis and is defined as the opposite of $\hat{z}$. The half-angle cone aperture was θ_0 = 30 deg.

The unitary vector $\hat{r}$ defined the LiDAR beam pointing direction in each LoS measurement during the LiDAR scan. In what follows, $\hat{r}$ is given in spherical coordinates relative to the moving coordinate system. Specifically, $\hat{r}$ is given by the zenith angle relative to $\hat{h}$, which is denoted θ_0 (i.e., the cone aperture), and by the azimuth angle relative to $\hat{x}$, which is denoted ϕ (Figure 1). As mentioned, θ_0 is the constant value of 30 deg corresponding to the scanning-cone aperture. ϕ is a time-variable angle representing the LiDAR scanning phase (positive towards $\hat{y}$).

During the LiDAR scan, the vector $\hat{r}$ rotated around $\hat{h}$ with a uniform circular motion at a rate of 1 revolution per second, i.e., $\phi(t) = 2\pi \times t$ [rad]. In what follows, for simplicity,

we use the variable ϕ instead of the usual time variable t. The variable ϕ ranged from 0 to 2π [rad] during a LiDAR scan. Therefore, $\hat{r}$ can be formulated in the moving coordinate system as follows:

$$\hat{r}(\phi) = \sin(\theta_0) \cdot \cos(\phi - \phi_0)\hat{x} + \sin(\theta_0) \cdot \sin(\phi - \phi_0)\hat{y} - \cos(\theta_0)\hat{z}, \tag{12}$$

where ϕ_0 is the LiDAR initial scan phase or, hereafter, the "initial phase".

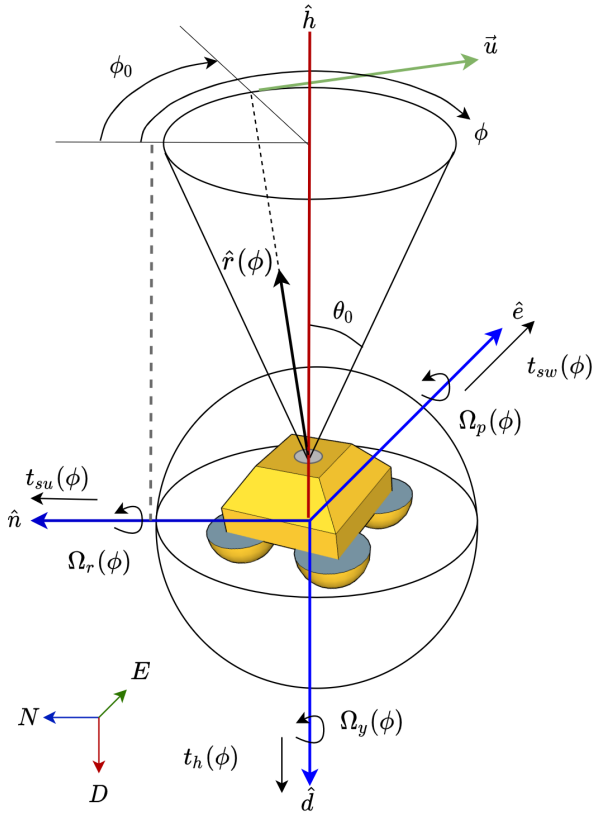

Figure 1. The motion geometry of the FDWL buoy.

3.4. The VAD Algorithm as a First-Order Fourier Series

Focusable CW DWLs use the VAD algorithm to retrieve the wind vector from the *measured* along-LoS-projected wind velocity during the LiDAR scan, which is computed as the so-called *VAD function*,

$$f(\phi) = \vec{u} \cdot \hat{r}(\phi). \tag{13}$$

In a motionless uniform nonturbulent wind scenario, the wind vector can be decomposed as $\vec{u} = HWS\hat{\rho} + w\hat{h}$, where $\hat{\rho} = cos(WD)\hat{x} + sin(WD)\hat{y}$, with WD as positive counterclockwise. Then, the ideal VAD function $f(\phi)$ takes the shape of the *model* cosine function [16,47],

$$f_{model}(\phi) = A \cdot cos(\phi - B) + C, \tag{14}$$

where A is the amplitude, B is the phase, and C is the offset term. From Equation (14) above, the HWS, WD, and VWS components of the wind vector are obtained as [28]

$$\begin{aligned} HWS &= \frac{A}{sin(\theta_0)}, \\ WD &= B, \\ VWS &= \frac{C}{cos(\theta_0)}. \end{aligned} \tag{15}$$

In Equation (15) above, the HWS, WD, and VWS refer to the values retrieved at the *i-th* scan.

The VAD algorithm uses the least squares (LSQ) algorithm to fit the model cosine function f_{model} (Equation (14)) to the measured function $f(\phi)$ in order to obtain the sought-after parameters A, B, and C:

$$min\Big|_{A,B,C}\Big\{\big|\big|f(\phi)-[A\cdot cos(\phi-B)+C]\big|\big|^2\Big\}. \tag{16}$$

The LSQ fit is usually carried out by means of numerical methods. Yet, they do not allow the explicit analytical formulation of solving coefficients A, B, and C with a view to understanding the propagation of the motion-induced error. A way out of this problem is to treat the error-norm minimization of Equation (16) in the Hilbert space of the square integrable functions $L^2[0,2\pi]$, in which $\{1,\cos(m\phi),\sin(n\phi)\}$, $m,n=1\ldots\infty$ form an orthogonal basis. Equivalently, the Fourier series is the LSQ projection of a target function to an orthogonal space defined by the sum of the sine and cosine functions [48]. Therefore, the solution of Equation (16) is the first-order Fourier series of $f(\phi)$ in the basis function $\{1,\cos(\phi),\sin(\phi)\}$. The first-order Fourier series can be rewritten in the form of Equation (14), in which the A, B, and C parameters can be expressed as a function of the Fourier coefficients as [49]

$$\begin{aligned} A &= \sqrt{a_1^2+b_1^2},\\ B &= arctan\left(-\frac{b_1}{a_1}\right),\\ C &= \frac{a_0}{2}, \end{aligned} \tag{17}$$

where a_0, a_1, and b_1 are the first-order Fourier coefficients of $f(\phi)$, obtained as [50]

$$\begin{aligned} a_0 &= \frac{2}{P}\int_0^P f(\phi)d\phi,\\ a_1 &= \frac{2}{P}\int_0^P f(\phi)\cos(\phi)d\phi,\\ b_1 &= \frac{2}{P}\int_0^P f(\phi)\sin(\phi)d\phi, \end{aligned} \tag{18}$$

where $P=2\pi$.

From Equations (15) and (17) above, it emerges that the Fourier coefficients a_1 and b_1 propagate errors to the HWS and WD (i.e., to the wind horizontal components), while the coefficient a_0 propagates errors only to the retrieved VWS.

As mentioned, homodyne-detection LiDARs, as in the case of the ZephIR 300, are only able to measure the magnitude of the along-LoS radial velocities but not the sign. This is equivalent to saying that $f(\phi)$ takes the shape of a rectified cosine, i.e., the absolute value of $f(\phi)$ [28]. When applying the VAD algorithm to $|f(\phi)|$, parameters A and C retain the same value as for the heterodyne case (VAD applied to $f(\phi)$), but B has a $\pm\pi$ rad ambiguity. The latter can be disambiguated by the wind vane co-located with the LiDAR buoy.

3.5. Estimation Error Methodology

In the absence of buoy motion, the X, Y, and Z axes of the moving coordinate system would coincide with the N, E, and D axes of the fixed system [23]. In the presence of waves, the FDWL experiences angular and translational motion around the three NED axes. In this section, we formulate analytical expressions for the motion influence on the VAD-retrieved wind vector.

In order to simplify the obtained analytical expressions, the following assumptions are considered: (i) the motion in each of the six DoF is considered to be a zero-mean simple harmonic motion; (ii) the rotational and translational motions are considered to be

independent error sources; and (iii) under motion, the VWS contribution to the HWS error is considered to be null as compared to the HWS contribution [51].

3.5.1. Rotational Motion Model

The FDWL buoy undergoes roll, pitch, and yaw motions around the three fixed coordinate axes, i.e., N, E, and D, respectively. As observed experimentally [23], roll and pitch motions can be modeled using a first-order small-angle approximation as simple harmonic motions. The *yaw motion,* which shows larger and more constant values with time, can be modeled by the *constant tilt.*

We define roll and pitch tilts (in units of radians) as sinusoidal signals of the form

$$\Omega_x(\phi) = A_x \cdot \sin(f_x\phi - \alpha_x), \tag{19}$$

where A_x, f_x, and α_x denote the amplitude, frequency, and motional phase, respectively. Subindex $x = roll, pitch$ denotes the *roll* and *pitch* motion, respectively. Note that, for convenience, Equation (19) is expressed as a function of the LiDAR scan-phase variable ϕ ($\phi = 2\pi t$) instead of time variable t.

As mentioned, the yaw tilt is considered a constant value $\Omega_{yaw}(\phi) = A_{yaw}$. This is conducted without limiting the general formulation of the problem. Thus, the reader could extend the formulation of the yaw angle to the harmonic case by defining the yaw motion as a sinusoidal signal (Equation (19)) plus an offset term equal to its mean value during the interval under study, and by following the formulas in Section 3.5.1 and Appendix A.1.

First, in order to compute the rotated LiDAR pointing direction, $\hat{r}_{rot}$, in the fixed NED coordinate system given the roll, pitch, and yaw rotations, we used the Euler rotation matrix. Euler's rotation theorem states that any rigid-body rotation can be defined by three rotation angles [52]. There are many different conventions regarding the rotation angles and their order of application. Here, we considered the NED convention, i.e., three elemental rotations were carried out sequentially: first, a rotation around the N axis (roll motion); second, a rotation around the E axis (pitch motion); and finally, a rotation around the D axis (yaw motion). The rotations were positive counterclockwise. Therefore, the Euler rotation matrix can be written as [53]

$$\boldsymbol{R} = \boldsymbol{R_D} \cdot \boldsymbol{R_E} \cdot \boldsymbol{R_N}, \tag{20}$$

where $\boldsymbol{R_N}$, $\boldsymbol{R_E}$, and $\boldsymbol{R_D}$ are the elemental rotation matrices around the N, E, and D axes, respectively. They can be formulated as follows:

$$\begin{aligned}
\boldsymbol{R_D} &= \begin{bmatrix} \cos(\Omega_y) & -\sin(\Omega_y) & 0 \\ \sin(\Omega_y) & \cos(\Omega_y) & 0 \\ 0 & 0 & 1 \end{bmatrix}, \\
\boldsymbol{R_E} &= \begin{bmatrix} \cos(\Omega_p(\phi)) & 0 & \sin(\Omega_p(\phi)) \\ 0 & 1 & 0 \\ -\sin(\Omega_p(\phi)) & 0 & \cos(\Omega_p(\phi)) \end{bmatrix}, \\
\boldsymbol{R_N} &= \begin{bmatrix} 1 & 0 & 0 \\ 0 & \cos(\Omega_r(\phi)) & -\sin(\Omega_r(\phi)) \\ 0 & \sin(\Omega_r(\phi)) & \cos(\Omega_r(\phi)) \end{bmatrix},
\end{aligned} \tag{21}$$

where subindexes y, p, and r stand for the "yaw", "pitch", and "roll", respectively.

The small-angle approximation for roll and pitch angles [23,28] translates into a first-order Taylor approximation for the sine and cosine functions (i.e., $sin(x) \simeq x$ and $cos(x) \simeq 1$). These first-order approximations were incorporated into Equation (A1), Appendix A.1, in order to simplify the rotation matrix $\boldsymbol{R}$.

The second step was to compute the rotated version of the LiDAR pointing vector, $\hat{r}_{rot}(\phi)$, in the NED fixed coordinate system:

$$\hat{r}_{rot}(\phi) = \boldsymbol{R} \cdot \hat{r}(\phi). \tag{22}$$

Third, the FDWL-measured wind under rotational motion was computed by projecting the wind vector over the rotated LiDAR pointing vector for each LoS. This was expressed by means of the dot product as follows:

$$f_{rot}(\phi) = \vec{u} \cdot \hat{r}_{rot}(\phi). \tag{23}$$

Eventually, the motion-corrupted FDWL wind vector was derived by applying the VAD algorithm to the function $f_{rot}(\phi)$ above. With this aim, the first-order Fourier coefficients of $f_{rot}(\phi)$ (i.e., a_0^{rot}, a_1^{rot}, and b_1^{rot}) were computed through Equation (18) by substituting $f_{rot}(\phi)$ in place of $f(\phi)$. The HWS retrieval error was computed as the difference between the "true" HWS (i.e., without motion influence) and the FDWL-retrieved HWS under rotational motion:

$$\epsilon_{HWS,i}^{rot} = HWS, i - \frac{1}{\sin(\theta_0)} \sqrt{(a_1^{rot})^2 + (b_1^{rot})^2}, \tag{24}$$

where a_1^{rot} and b_1^{rot} are the Fourier coefficients of $f_{rot}(\phi)$. See Appendix A.3 for the mathematical results in expanded form.

3.5.2. Translational-Motion Model

Waves also induce translational motion to the FDWL in the N, E, and D directions, i.e., surge, sway, and heave motions, respectively. Similar to the derivation of the rotational motion components in Equation (19), sinusoidal variation was assumed for each translational-motion component. They were formulated as follows:

$$t_x(\phi) = A_x \cdot \sin(f_x \phi - \alpha_x), \tag{25}$$

where A_x, f_x, and α_x, are the amplitude, frequency, and phase of the translational motion x, where x denotes the surge, sway, or heave components. We also defined the translational-velocity vector $\vec{t}(\phi)$ in the NED fixed coordinate system as the three-component vector,

$$\vec{t}(\phi) = [t_{su}(\phi), t_{sw}(\phi), t_{he}(\phi)], \tag{26}$$

where the subscripts su, sw, and he referred to the *surge*, *sway*, and *heave*, respectively.

First, to compute the FDWL-measured wind under translational motion, we computed the apparent wind vector. The apparent wind vector measured by the FDWL was the difference between the wind vector and the translational-velocity vector:

$$\vec{u}^{trans}(\phi) = \vec{u} - \vec{t}(\phi). \tag{27}$$

Second, the translational-velocity contribution to the LiDAR-measured LoS, $f_{trans}(\phi)$, was obtained by projecting the apparent wind vector, $\vec{u}^{trans}$, on the LiDAR pointing direction $\hat{r}(\phi)$ as follows:

$$f_{trans}(\phi) = \vec{u}^{trans}(\phi) \cdot \hat{r}(\phi). \tag{28}$$

The LiDAR-retrieved wind vector was the result of applying the VAD algorithm over the motion-corrupted LoS, $f_{trans}(\phi)$. The Fourier coefficients a_0^{trans}, a_1^{trans}, and b_1^{trans} were obtained through Equation (18) by substituting $f(\phi)$ by $f_{trans}(\phi)$. The Fourier coefficients are given in expanded form in Appendix A.4 of Appendix A.

Finally, the HWS measurement error due to the FDWL's translational motion $\epsilon_{HWS,i}^{trans}$ became

$$\epsilon^{trans}_{HWS,i} = HWS_i - \frac{1}{\sin(\theta_0)}\sqrt{(a_1^{trans})^2 + (b_1^{trans})^2}. \quad (29)$$

3.5.3. Total Error Model

In order to estimate the total error, we departed from the assumption that the rotational and translational motion were independent error sources (see Section 3.5). Therefore, the total error in the retrieved HWS in a LiDAR scan is the superposition of errors:

$$\epsilon_{HWS,i}(\vec{u}, \phi_0) = \epsilon^{rot}_{HWS,i}(\vec{u}, \phi_0) + \epsilon^{trans}_{HWS,i}(\vec{u}, \phi_0). \quad (30)$$

In Equation (30), the total error, $\epsilon_{HWS,i}(\vec{u}, \phi_0)$, is parameterized by the instantaneous wind vector $\vec{u}$ and initial phase ϕ_0.

Figure 2a illustrates the estimated HWS total error in a LiDAR scan parameterized as a function of the wind direction (WD ranging from 0 to 360 deg) and the initial phase ϕ_0 in a roll-only motion scenario ($HWS = 10$ m/s, $VWS = 0$ m/s). As can be observed, the HWS error was highly dependent on both input parameters (WD and initial phase), ranging from -1.5 up to 1.5 m/s (the HWS errors for other input HWSs are scalable through simple direct proportionality). If the WD is known, the HWS error in a LiDAR scan is dependent only on the initial phase. This is represented in Figure 2b, where the HWS error in the LiDAR scan in Figure 2a is represented as a function of the initial phase ϕ_0 for the constraint settings $HWS = 10$ m/s, $WD = 275$ deg, and $VWS = 0$ m/s.

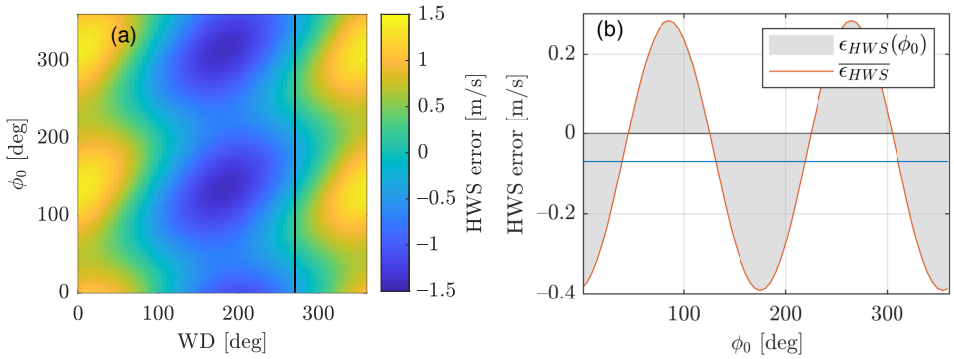

Figure 2. Example of the estimation of the HWS total error in a LiDAR scan ($HWS = 10$ m/s, $VWS = 0$ m/s, and a WD ranging from 0 to 360 deg, roll-only motion). (**a**) Color plot of the HWS error as a function of the wind direction, WD, and initial phase, ϕ_0. (**b**) HWS error for $WD = 275$ deg (vertical black line in panel (**a**)) as a function of the initial phase. The blue horizontal line indicates the mean HWS error.

However, the initial phase is the manufacturer's undisclosed parameter for the ZephIR 300 LiDAR. As the instantaneous value of the initial phase at each LiDAR scan cannot be known nor, consequently, the total error, we assumed the initial phase was a random variable with a uniform distribution between 0 and 2π rad [25]. As a result, HWS error moments rather than instantaneous values were derived.

The 10 min HWS *bias* (Equation (5)) was computed as the expectation (first raw moment) of the HWS total error function (Equation (30)), $\epsilon_{HWS,i}(\vec{u}, \phi_0)$, with respect to the initial phase, ϕ_0, constrained to the mean wind vector $\vec{U}$ as follows:

$$bias_{est} = E_{\phi_0}[\epsilon_{HWS,i}(\vec{U}, \phi_0)]. \quad (31)$$

In practice, the $bias_{est}$ is simply the mean value of $\epsilon_{HWS,i}(\vec{U}, \phi_0)$ computed as $bias_{est} = \frac{1}{N}\sum_{i=1}^{N} \epsilon_{HWS,i}(\vec{U}, \phi_{0,i})$, where the discrete random variable ϕ_0 is defined by a finite list $\{\phi_{0,1}, \ldots, \phi_{0,N}\}$ of equally likely outcomes (vertical line in Figure 2a).

Analogously, the 10 min *TI increment* of Equation (7) is estimated as follows:

$$\Delta TI_{est} = \frac{STD_{\phi_0}[\epsilon_{HWS,i}(\vec{U}, \phi_0)]}{\hat{HWS}}, \tag{32}$$

where STD stands for the standard deviation, which is the square root of the variance of the total error ($\sigma_{\epsilon_{HWS,i}}$), and $\hat{HWS}$ is the 10 min mean HWS measured by the FDWL.

3.6. Bias and TI-Increment Estimation Procedure

Figure 3 summarizes the procedure described in Section 3.5 to compute the estimated 10 min bias and TI increment. The 10 min mean wind vector ($\vec{U}$), as well as the characteristic amplitude, frequency, and phase of each of the 6 DoF, were the inputs. In practice, the yaw frequency and phase were set to zero. The Fourier coefficients a_1^{rot} and b_1^{rot} were obtained through Equations (A3) and (A4), respectively, which estimated the HWS measurement error due to the *rotational* motion ($\epsilon_{HWS,i}^{rot}$, Equation (24)). Similarly, the Fourier coefficients a_1^{trans} and b_1^{trans} were obtained through Equations (A5) and (A6), respectively, which estimated the HWS measurement error due to the *translational* motion ($\epsilon_{HWS,i}^{trans}$, Equation (29)). The following step was to sum the rotational- and translational-error expressions to yield the total error as a function of the wind vector and initial scan phase (Equation (30)). Then, it was constrained to the 10 min mean wind vector, $\vec{U}$, by substituting the $\vec{u}$ in Equation (30) with $\vec{U}$. Finally, the bias and TI increment were estimated by means of Equations (31) and (32), respectively.

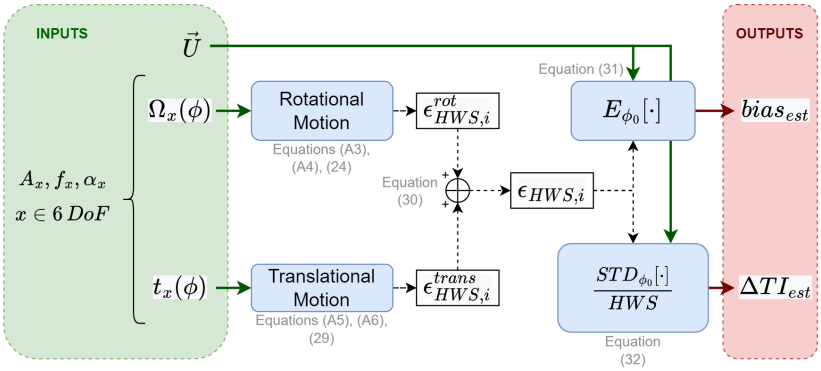

Figure 3. Block diagram depicting the Section 3.5 estimation procedure for the bias and TI increment.

Alternatively, for a specific 1 s error model validation (refer to Section 4.1), the total error (Equation (30)) was obtained as a function of the instantaneous wind vector and the LiDAR initial scan phase.

3.7. Sinusoidal Characterization of the Measured Motion Time Series

In order to estimate the FDWL motion-induced error with the presented methodology based on Equations (19) and (25), there is a requirement that the motion time series in each of the DoF be modeled as a sinusoidal signal with a characteristic amplitude, frequency, and phase (A, f, and α, respectively). The estimation procedure for these parameters is described next through a case example.

Figure 4a shows a record of the IMU-measured roll time series during the PdP campaign. As can be noticed, the signal was composed of multiple frequency components. To analyze the signal spectrum, the power spectral density (PSD) was computed in batches of 10 min segments using the Blackman–Tukey method [54]. In Figure 4b, it emerges that the signal had a broad spectrum with relevant frequency components from approximately 0.25 to 0.5 Hz. The characteristic frequency f was computed as the frequency corresponding to the peak PSD maximum ($\simeq$0.3 Hz).

In order to estimate the characteristic amplitude A, we made use of the fact that the amplitude of a sinusoidal signal is related to its power, P, through the relationship

$P = A^2/2$ [54]. Moreover, the mean power $\overline{P}$ of a stochastic signal $s(t)$ (i.e., the IMU-measured motion) with duration T is computed as [54]

$$\overline{P} = \int_0^T |s(t)|^2 dt. \tag{33}$$

The mean power, $\overline{P}$, takes into account all the frequency components of the signal spectrum [55]. Therefore, the characteristic amplitude was estimated from the mean signal power as $A = \sqrt{2\overline{P}}$. Finally, the characteristic phase α was obtained from the first-order Fourier decomposition of $s(t)$ in a similar fashion to the calculation of phase term B in Equation (17), given the first-order coefficients a_1 and b_1 in Equation (18) (see Section 3.4).

Figure 4a shows the IMU-measured roll time series against the "fitted" sinusoidal signal with the characteristic amplitude, frequency, and phase of $A = 1.3$ deg, $f = 0.3$ Hz, and $\alpha = 1.1$ deg, respectively. It can be observed that the fitted sinusoidal signal reproduced the measured time series under a first-harmonic approximation with reasonable accuracy.

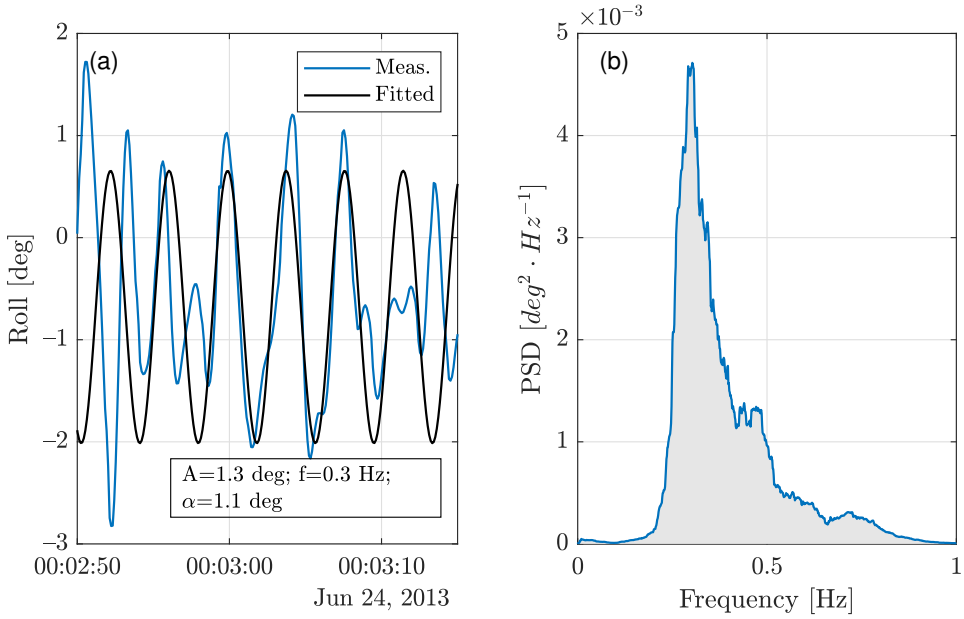

Figure 4. The FDWL motion characterization as a sinusoidal signal: roll motion example (PdP, 24 June 2013, 00:00 LT). (**a**) The 10 min roll time series (blue trace) and fitted sinusoidal signal (black trace). (**b**) PSD of the panel (**a**) time series.

3.8. A Note on Appendix A and the Supplementary Materials Math Formulations

Provided in Appendix A is a formulation compendium to compute the 6-DoF-motion-induced error (Sectioin 3.5.3). A MATLAB^{TM} R2020a code to compute the total error (Sectioin 3.5.3) is also included as part of the Supplementary Materials of this manuscript.

The mathematical derivations of this Appendix A were checked both algebraically and numerically. Algebraically, the manually derived math expressions were validated using the MATLAB^{TM} R2020a symbolic toolbox. Numerically, these expressions were coded in MATLAB and compared with the outputs of the FDWL simulator [35] (Figures 5–7) for quality assurance.

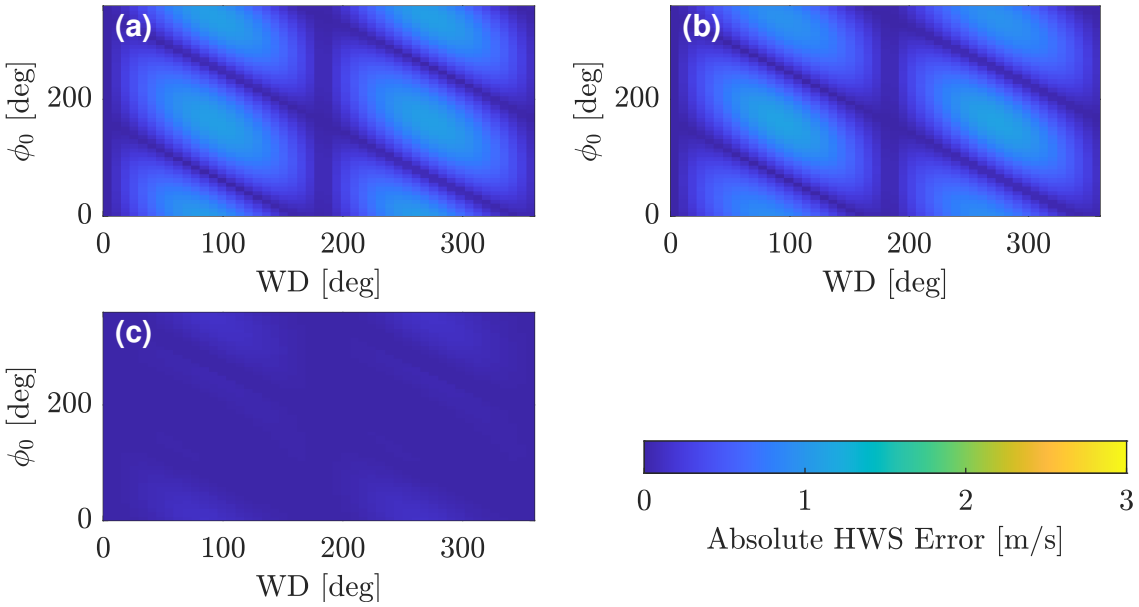

Figure 5. Validation of the analytical-error formulation in the roll-only scenario #1: *HWS error* (parameters: $A_{roll} = 10$ deg, $f_{roll} = 0.3$ Hz and $\alpha_r oll = 0$ deg. Input wind: $HWS = 10$ m/s, $VWS = 0$ m/s). (**a**) The analytically estimated *HWS* error as a function of the wind direction (WD) and the initial scan phase (ϕ_0). (**b**) The simulator-estimated *HWS* error. (**c**) The difference of (**a**) minus (**b**) (in absolute value).

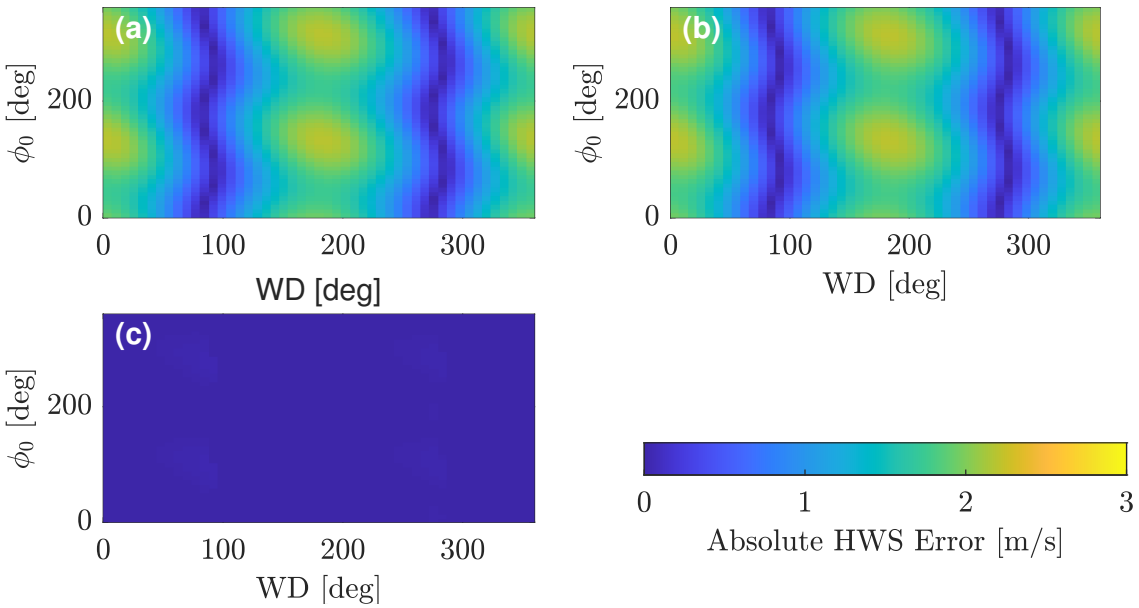

Figure 6. Validation of the analytical-error formulation in the translational-only scenario #2: *HWS error* (parameters: $A_{surge} = 10$ deg). (**a**) The analytically estimated *HWS* error as a function of the wind direction (WD) and the initial scan phase (ϕ_0). (**b**) The simulator-estimated *HWS* error. (**c**) The difference of (**a**) minus (**b**) (in absolute value).

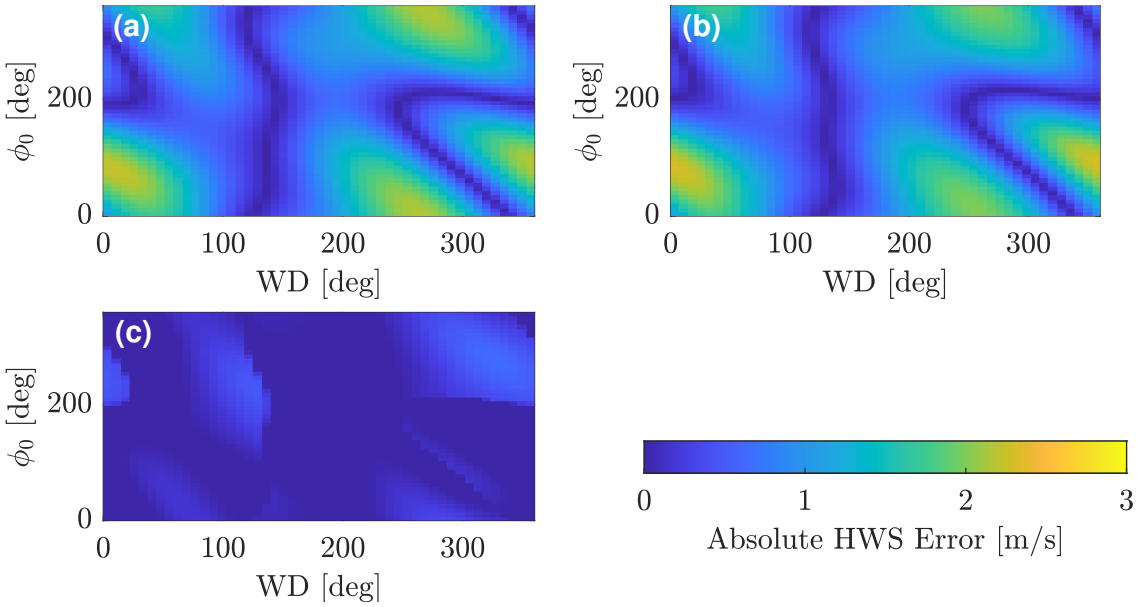

Figure 7. Validation of the analytical-error formulation in the 6 DoF scenario #3: *HWS error* (parameters: $A_{roll} = A_{pitch} = 10$ deg, and $A_{surge} = A_{sway} = A_{heave} = 2$ m/s). (**a**) The analytically estimated *HWS* error as a function of the wind direction (WD) and the initial scan phase (ϕ_0). (**b**) The simulator-estimated *HWS* error. (**c**) The difference of (**a**) minus (**b**) (in absolute value).

4. Results and Discussion

4.1. Error Model Validation

In order to validate the presented *analytical-error* formulation (Section 3.5 and Appendix A; in what follows, "the unified-error formulation"), the estimated total error in the FDWL-retrieved *HWS* (Equation (30)) was compared with the LiDAR motion simulator as a reference [37]. The study was carried out by inputting the same reference wind vector ($HWS = 10$ m/s and $VWS = 0$ m/s) into both the unified formulation and the simulator under three different motion scenarios: (i) rotational motion only, (ii) translational motion only, and (iii) 6 DoF motion. In all cases, $f_x = 0.3$ Hz and $\alpha_x = 0$ deg, $x = roll, pitch$ were used. In each scenario, the performance of the analytically estimated error was evaluated as a function of the *WD* and initial scan phase ϕ_0.

In *roll-only scenario #1* (Figure 5), the analytically estimated error (Figure 5a, Equation (24)) was virtually identical to the simulator-estimated error (Figure 5b) over the whole span of the *WD*s and the initial-phase values. From Figure 5c, all the error differences between panels (a) and (b) were lower than 0.3 m/s, which is evidence of the satisfactory accuracy attained using the first-order approximation in the formulation. The *RMSE* between the error estimates of Figure 5a,b (equivalently, the square root of the mean of the squares of the error values shown in Figure 5c) was 0.04 m/s.

When addressing the *translational-only scenario* #2 (Figure 6), null differences (0 m/s) were found in Figure 6c between the analytically estimated and the simulator-estimated error. The exact 0 m/s error difference was explained by the fact that no approximations were used when deriving the analytical expressions for the translational-motion component.

Opposite to other floating remote-sensing devices such as high-frequency surface-wave radars, which measure the horizontal propagation of waves and thus are not sensitive to heave-induced Doppler effect [56,57], the ZephIR^{TM} 300 FDWL is sensitive to all three translational motion components due to its inherent conical scanning pattern [16].

Finally, the successful performance of the unified formulation presented for the analytically estimated error was re-encountered in Figure 7, where both the translational and rotational motion were combined into the 6 DoF motion *scenario #3*. Despite the greater

complexity of this scenario, the error differences (Figure 7c) remained below 0.7 m/s. The $RMSE$ was 0.22 m/s.

4.2. Experimental Results

The unified-error formulation (Section 3.5 and Appendix A) was also validated by comparing the analytically estimated HWS mean bias and TI increment (Equations (31) and (32), respectively) against their experimental values (Equations (4) and (6), respectively). The experimental values were computed from the 10 min errors between the FDWL and the reference fixed LiDAR used in both the nearshore ("Pont del Petroli") and open-sea (IJmuiden) scenarios. For the IJmuiden campaign, the measurements of the FDWL at 83 m and the measurements of the metmast DWL at 92 m were considered. Towards this purpose, 848 data records (6 to 30 June 2013) from PdP campaign and 3893 data records (1 April to 7 May 2015) from the IJmuiden campaign were used (see Section 2). The data were filtered for quality assurance following the outlier-rejection criteria [33]: the measured HWS values outside the 1–80 m/s range, the rain-flagged data, the spatial variation (SV) values higher than 0.2, and the backscatter coefficients lower than 0.02 were removed. The SV is an indicator of the goodness of the VAD fitting of the measured LoS in a LiDAR scan [58]. The backscatter coefficient is indicative of the power of the received LiDAR echo.

4.2.1. The Performance according to the Estimation of the HWS Bias

In the PdP campaign, using statistical analysis, the measured 10 min HWS bias (Equation (4)) showed virtually nil values in accordance with the previous results in nearshore locations in the state of the art [27,28]. The median of the measured 10 min HWS bias was -0.02%, with 25th and 75th percentiles of -0.89% and 0.76%, respectively. On the other hand, the analytically estimated 10 min HWS bias (Equation (5)) showed values of the same order of magnitude as the measured ones, thus validating the method. Thus, the median of the estimated bias was 0.06%, and the 25th and 75th percentiles were -0.66%, and 0.64%, respectively. The median bias was in accordance with the results obtained in other state-of-the-art studies [38].

In the Ijmuiden campaign, the measured 10 min HWS showed higher values than the observed ones in the "Pont del Petroli" campaign: the median of the measured 10 min HWS bias was -0.53%, with 25th and 75th percentiles of -2.30% and 1.08%, respectively (and notice the asymmetrical distribution of these percentiles around 0%). These values were in accordance with the previous open-sea measurement campaigns [32,59]. This is due to the fact that in an open-sea scenario there is stronger wave motion, which induces a higher error in the FDWL measurements. The abovementioned asymmetry on the measured biases accounts for the wind shear between the fixed DWL and FDWL measurement heights (92 and 83 m, respectively). The analytical model estimated biases of the same order of magnitude as the measured ones with a median of 0.05%, and 25th and 75th percentiles of -1.48% and 1.47%, respectively, which further validated the analytical model.

4.2.2. Performance according to the Estimation of the TI Increment (I): Case Example

As part of the validation study, in the next case example, the *analytically estimated* 10 min TI increment, ΔTI_{est} (Equation (32)), was compared with the *measured* one, ΔTI_{meas} (Equation (7)). The different motion conditions studied are described as a function of the *mean tilt amplitude* and *mean translational-velocity amplitude* of the LiDAR buoy.

The *mean tilt amplitude* was computed as the 10 min mean of the quadratic sum of roll and pitch tilts (simple harmonic motion, Equation (19)) [28]. It can be formulated as follows:

$$\overline{A_{tilt}} = \frac{\sum_{k=1}^{N} \sqrt{\Omega_{roll}(k)^2 + \Omega_{pitch}(k)^2}}{N}, \tag{34}$$

where Ω_x, $x = roll pitch$ is the IMU-measured roll/pitch tilt, $N = 6000$ is the number of samples in a 10 min interval at a 10 Hz IMU-sampling frequency, and k is a reminder of the discrete time t_k.

The *mean translational-velocity amplitude* was computed as the 10 min mean norm of the FDWL translational-velocity vector,

$$\overline{A_{v_{trans}}} = \frac{\sum_{k=1}^{N} ||\vec{t}(k)||}{N}, \tag{35}$$

where $\vec{t}(k)$ is the translational-velocity vector defined by Equation (26).

Figure 8a compares the estimated TI-increment time series (ΔTI_{est}) with the measured one (ΔTI_{meas}) in the context of the PdP campaign. The motion-induced error on the FDWL-measured TI manifested as TI increments between 0.5 and 5%. The highest TI increments occurred during the daytime (from 10 a.m. to 4 p.m., approximately), corresponding to time periods with high HWSs. These periods were also related to the high wave motion [27,60]. This was corroborated by Figure 8b, where the mean tilt amplitude and mean translational-velocity amplitude of the floating LiDAR are depicted as time series. It can be observed that the high TI-increment values in Figure 8a were linked to high-motion scenarios, i.e., to the time periods with high tilt and velocity amplitudes in Figure 8b.

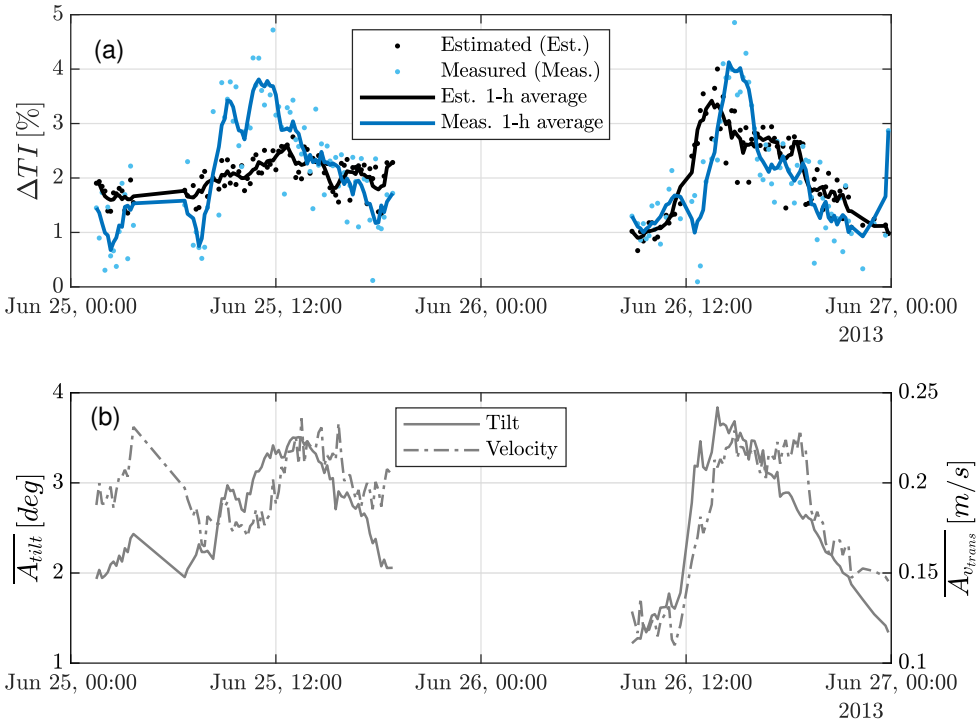

Figure 8. Validation of the analytical-error formulation in a real case scenario (PdP campaign, 25 June 2013, 00:00 UTC to 27 June 2013, 00:00 UTC): *TI increment*. (**a**) The analytically estimated vs. the measured TI-increment time series. The black dots represent the 10 min analytically estimated TI increment, ΔTI_{est} (Equation (7)). The blue dots represent the 10 min measured TI increment, ΔTI_{meas} (Equation (6)). (**b**) The mean tilt amplitude (Equation (34)) and the mean translational-velocity amplitude (Equation (35)) time series. In both panels, the solid trace represents the 1 h averaged time series.

As shown in Figure 8a, the estimated TI increment exhibited similar values to the measured ones over the period under study. The 1 h averaged time series further showed the goodness of the TI-increment estimates. However, a small underestimation of the peak values occurred. Thus, while the measured TI increment peaked at 5% close to noon, the estimated one only reached 3.5%. Larger differences were observed in one-to-one comparisons of the 10 min estimates with the 10 min measurements. A suitable explanation for this is that in the unified formulation presented in Section 3.5.3, the wind flow during

10 min periods was assumed to be uniform, and only the motion influence was considered. As the LiDARs were located 50 m apart, wind scenarios with high spatial variability (e.g., turbulent winds coming from the urban area, Section 2) usually led to different instantaneous measurements between the floating and the reference LiDAR. Therefore, the correlation coefficients $\rho_{F,R} < 1$ (Section 3.2.1) may limit the validity of the estimates, ΔTI_{est}. This effect may also occur in low-motion scenarios [33].

4.3. The Performance of the Estimation of the TI Increment (II): Statistical Analysis

The performance of the analytical-error formulation when estimating the 10 min TI increment was also assessed with reference to the FDWL-measured TI increment under nearshore and open-sea motional scenarios (the PdP and IJmuiden campaigns, respectively). The statistical sample consisted of 848 data records (from 6 to 30 June 2013) for the PdP campaign and 3893 data records (from 1 April to 7 May of 2015) for the IJmuiden campaign. The estimated and the measured TI increments (ΔTI_{est} and ΔTI_{meas}, respectively) for the whole campaign were clustered as a function of the wind intensity, using the *HWS* as the binning variable, and as a function of the type of motion (i.e., rotational or translational), using the *mean tilt amplitude* and the *mean translational-velocity amplitude* as the respective binning variables.

The estimation accuracy was quantitatively assessed according to the root mean square error ($RMSE$), which is formulated as follows:

$$RMSE = \sqrt{\frac{\sum_{p=1}^{N}[\Delta TI_{est}(p) - \Delta TI_{meas}(p)]^2}{N}}, \tag{36}$$

where N is the number of samples in the bin under study, $\Delta TI_{est}(p)$ is the *p-th* TI-increment estimate in the bin, and $\Delta TI_{meas}(p)$ is the corresponding *p-th* measurement.

Figure 9 depicts the statistical results for the PdP (left panels) and IJmuiden (right panels) campaigns. In all panels, it can be observed that the TI increment, ΔTI, was always positive, evidencing the motion-induced additive turbulence [26,28]. Moreover, it increased with increasing wave motion, i.e., with increasing mean tilt amplitude (panels (a), (b)) and mean translational-velocity amplitude (panels (c), (d)). ΔTI ranged from median values of $\Delta TI \simeq 1\%$ in low-motion scenarios to $\Delta TI \simeq 2\%$ in high-motion ones. The green bars illustrating the statistically significant bins (i.e., bins containing greater than or equal to 5% of the population of the PdP campaign, i.e., $\simeq$50 samples) showed mean tilt amplitudes between 1 and 3.5 deg for the PdP campaign and between 1 and 5.5 deg for the IJmuiden campaign (notice the different X-axis ranges used). The observed mean translational-velocity amplitudes ranged between 0.1 and 0.2 m/s for the PdP campaign and between 0.1 and 0.65 m/s for the IJmuiden campaign (notice the different X-axis ranges used). The HWS ranged between 2 and 8 m/s in the PdP campaign and between 2 and 22 m/s in the IJmuiden campaign (notice the different X-axis ranges used). The higher motion and wind magnitudes evidenced the harsher scenario experienced by the FDWL during the IJmuiden campaign.

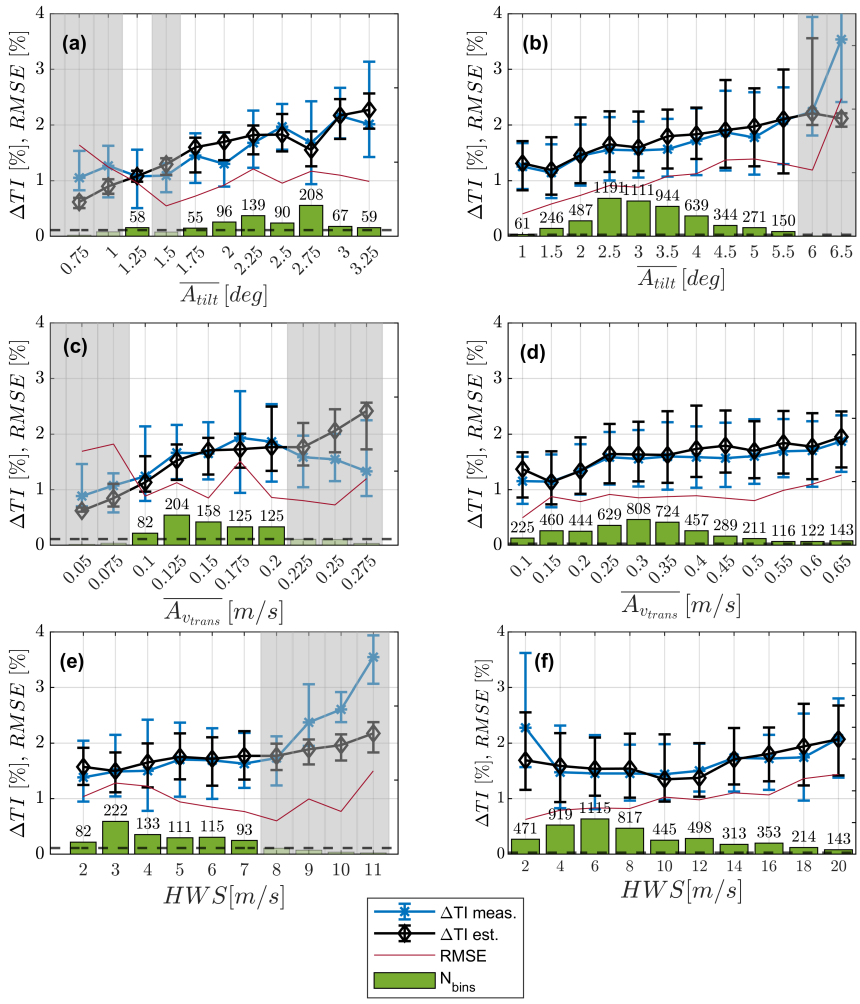

Figure 9. Validation of the analytical-error formulation: *Global statistics for the PdP campaign (6 to 30 June 2013) and IJmuiden campaign (1 April to 1 June 2015).* The left panels show the results obtained for the PdP campaign, and the right panels show the results obtained for the IJmuiden campaign, with the comparison between the measured and the estimated TI increment as a function of different motion conditions clustered by (panels (**a**,**b**)) *mean tilt amplitude* (rotational motion), (panels (**c**,**d**)) *mean translational-velocity amplitude*, and (panels (**e**,**f**)) *mean HWS*. The error bars indicate the 25th and 75th percentiles. The bar graphs represent the number of occurrences in the data for each category of bin. The solid red lines represent the $RMSE$ between ΔTI_{est} and ΔTI_{meas} for each category of bin. The bins containing less than 5% of the PdP population are gray shaded.

On one hand, Figure 9a,b plot the TI increment as a function of the mean tilt amplitude in 0.5 deg bins, which was representative of the *rotational-motion* component. The median of the estimated ΔTI values virtually matched that of the measurements, thus validating the overall analytical-error formulation. In the PdP campaign (Figure 9a), the error bars showed a larger dispersion for the measured values (ΔTI_{meas}) than for the estimated ones (ΔTI_{est}). This is attributable to the urban topology surrounding the experimental area, which creates a high spatial variation in the wind field. In contrast, this was not found in IJmuiden. Thus, Figure 9b,d,f shows estimated error bars virtually coincidental with the measured ones due to the more homogeneous wind fields found over the ocean.

On the other hand, Figure 9c,d represent the TI increment as a function of the FDWL mean *translational* velocity in 0.025 m/s bins for the PdP campaign and 0.05 m/s bins for the IJmuiden campaign, respectively. Similar to Figure 9a,b, the median of the estimated ΔTI values almost ideally matched the measurements in all the significant bins (dark green),

Figure 9c,d. The largest difference was $\Delta TI_{meas} - \Delta TI_{est} = 0.26\%$ for the 0.175 m/s bin. Similar comments apply to those for Figure 9a,b regarding the measurement error bars.

Finally, Figure 9e,f depict the TI increment as a function of the mean HWS in 1 m/s bins for the PdP campaign and 2 m/s for the IJmuiden campaign, respectively. Similar concurrent results were observed, with the estimated ΔTI median values matching the measurements for all HWS bins except for the 2 m/s one. This was due to the fact that the ZephIR^{TM} 300 HWS measurements below 3 m/s were tagged as "unreliable", according to the manufacturer's specs for the LiDAR [40]. Similar discussion comments apply for the error bars shown in Figure 9e,f.

The $RMSE$ between the estimated and the measured ΔTI (Equation (36)) is depicted in red for each of the tilt, velocity, and HWS bins. Similar values were obtained in all the statistically significant bins, ranging from $RMSE = 0.004$ (0.4%) up to $RMSE = 0.013$ (1.3%), which was comparable to (therefore, consistent with) the size of the measurement error bars obtained for ΔTI_{meas}. As can be observed, the $RMSE$ was slightly correlated with the tilt, so that the larger the buoy tilt, the larger the $RMSE$ in rough approximation, which in turn accounted for the first-order approximation used in Equation (A1) (refer to Appendix A.1).

5. Conclusions

A *unified analytical formulation* for the computation of the 6-DoF-motion-induced error in focusable CW FDWLs was presented (Figure 3). The total error in the retrieved HWS was computed as the superposition of the rotational- and translational-motion errors. The formulation proved to be capable of estimating the HWS bias (Section 4.2.1) and TI increment (Figures 8 and 9).

The analytical model departed from a thorough formulation of the FDWL buoy geometry and dynamics in order to derive the rotational- and translational-motion influence on the LiDAR-measured LoS measurements in a CW DWL scan. The well-known VAD algorithm was computed as a first-order Fourier series, which allowed derivation of the sought-after analytical expressions describing the FDWL-measured wind-vector error as a function of the buoy attitude and the "true" wind vector. The first-order approximation was retained when computing the buoy rotational matrix. The assumption of a uniformly distributed random initial scan phase permitted the estimation of the HWS measurement bias and $RMSE$ over 10 min time intervals.

The wave-induced motion in each of the six DoF was modeled as a simple harmonic motion with a characteristic amplitude, frequency, and phase recomputed every 10 min for each DoF. A method to estimate these variables based on spectral analysis of the LiDAR-buoy motional time series was presented in Section 3.7.

The proposed formulation was numerically validated by comparing the HWS error figures obtained as a function of the WD and the initial scan phase with those output by the FDWL motion simulator [37]. A virtually perfect match between both methods was found except for the second-order approximation errors.

The methodology was further validated using experimental data from the "Pont del Petroli" (Badalona, Barcelona) and IJmuiden (North sea, 85 km offshore the Netherlands) campaigns, in which an FDWL and a reference fixed LiDAR were used. The estimated 10 min bias using the analytical formulation presented here yielded similar results to the measured one. Thus, for the PdP campaign, the median values obtained for the estimated and the experimental HWS bias were -0.02% and 0.06%, respectively, and the 25th and 75th percentiles were -0.66% (estimated) and -0.89% (measured) and 0.76% (measured) and 0.64% (estimated), respectively. For the IJmuiden campaign, median values of -0.53% (measured) and 0.05% (estimated) were found, and the 25th and 75th percentiles were -2.30% (measured) and -1.48% (estimated) and 1.08% (measured) and 1.47% (estimated), respectively. The inherent asymmetry between the positive and negative biases was due to the wind shear between the fixed DWL and FDWL measurement heights. The slight differences between the measured and estimated values were inconsequential and were

due to the harsher sea conditions at the IJmuiden site. With regard to the estimation of the TI increment, the analytical estimates matched the measured values in statistical terms under all motion and wind scenarios for both the PdP and IJmuiden campaigns (Figure 9). Thus, the root mean square differences between the medians of ΔTI_{est} and ΔTI_{meas} were 0.16% (PdP) and 0.11% (IJmuiden) for the rotational motion (Figure 9a,b), 0.13% and 0.16% for the translational motion (Figure 9c,d), and 0.14% and 0.21% for the HWS (Figure 9e,f), giving mean values of about 0.015 (1.5%). The experimental validation was limited by the fact that the compared LiDARs were a minimum of 50 m apart and subject to wind flows that were not always uniform. This caused moderate dispersion in the turbulence values measured by the two LiDARs, which deteriorated in one-to-one comparison of the 10 min TI.

All in all, the unified formulation presented here proved to be a straightforward and accurate tool for quantitatively assessing the 6-DoF-motion-induced error in focusable CW FDWLs in terms of both the HWS-bias and TI-increment estimation, in addition to the real one. This information is increasingly being recognized as critical to the acceptance of FDWLs and ship-borne LiDARs in the Wind Energy industry as compared to fixed LiDARs and reference metmasts [61,62]. To the best of our knowledge, the proposed unified analytical formulation is the first in the state of the art able to estimate the TI increment at a 10-min basis from solely FDWL measurements under virtually all motional and wind scenarios. In addition, the novel analytical expressions obtained are less computationally demanding than numerical simulators and unveil a key understanding of the involved FDWL attitude and LiDAR-retrieval-algorithm error sources. These findings have important implications for the accurate measurement of wind speed and turbulence in FDWLs, particularly when they are being deployed as standalone measurement instruments. $Matlab^{TM}$ R2020a codes are also provided to the reader as part of the Supplementary Materials of this manuscript. Further steps could include the study of multimodal motion as well as the wind flow variability in a LiDAR scan. Finally, experimental validation would benefit from tests at different LiDAR sounding heights.

Supplementary Materials: The following are available online at https://www.mdpi.com/article/10.3390/rs15061478/s1.

Author Contributions: Derivation of analytical expressions, J.F.-G. and A.S.-B.; software development, A.S.-B. and M.P.A.d.S.; analyses and figures, A.S.-B. and J.F.-G.; writing—original draft preparation, A.S.-B., J.F.-G. and M.P.A.d.S.; review and editing, F.R.; funding acquisition, F.R.; conceptualization support, F.R. This work was developed as part of A.S.-B.'s doctoral thesis, supervised by F.R. and J.F.-G.'s master thesis co-advised by F.R. and A.S.-B. All authors have read and agreed to the published version of the manuscript.

Funding: This research project was part of the project PID2021-126436OB-C21 funded by the Ministerio de Ciencia e Investigación (MCIN)/Agencia Estatal de Investigación (AEI)/10.13039/501100011033 y FEDER "Una manera de hacer Europa". The work of A. Salcedo-Bosch was supported by grant 2020 FISDU 00455 funded by Generalitat de Catalunya—AGAUR. The work of M.P Araújo da Silva was supported under Grant PRE2018-086054 funded by MCIN/AEI/10.13039/501100011033 and FSE "El FSE invierte en tu futuro". The European Commission collaborated under projects H2020 ATMO-ACCESS (GA-101008004) and H2020 ACTRIS-IMP (GA-871115). The European Institute of Innovation and Technology (EIT), KIC InnoEnergy project NEPTUNE (call FP7), supported the measurement campaigns.

Data Availability Statement: Data are available from the authors.

Conflicts of Interest: The authors declare no conflict of interest.

Abbreviations

The following abbreviations are used in this manuscript:

CW	continuous wave
DoF	degrees of freedom
DWL	Doppler wind LiDAR
FDWL	floating Doppler wind LiDAR
HWS	horizontal wind speed
IMU	inertial measurement unit
LD	linear dichroism
LoS	line of sight
LSQ	least squares
NED	north–east–down
metmast	meteorological mast
MDPI	Multidisciplinary Digital Publishing Institute
PdP	Pont del Petroli
PSD	power spectral density
RMSE	root mean square error
SV	spatial variation
TI	turbulence intensity
VAD	velocity–azimuth display
VWS	vertical wind speed
WD	wind direction

Appendix A. Formulation Compendium

This Appendix provides exhaustive details for the formulation of the 6-DoF motion-induced error. Specifically, Appendix A.1 addresses the first-order approximation of the Euler rotation matrix, $\boldsymbol{R}$, in connection with Equations (20) and (21). Appendix A.2 provides the calculation of the LoS-projected wind vector under rotational motion to obtain the VAD function $f_{rot}(\phi)$. The first-order Fourier coefficients under rotational and translational motion are formulated in Appendices A.3 and A.4, respectively, by using the auxiliary integrals given in Appendix A.5. The Supplementary Materials provide the MATLAB^{TM} R2020a code to compute the total error (Section 3.5.3).

Refer to Section 4.1 and Figures 5–7 for quality assurance.

Appendix A.1. First-Order Approximation of the Rotation Matrix

The Euler rotation matrix, $\boldsymbol{R}$, is the result of elemental rotations about the N, E, and D axes, $\boldsymbol{R_N}$, $\boldsymbol{R_E}$, and $\boldsymbol{R_D}$, respectively, representing the roll, pitch, and yaw rotations. Inserting Equations (21) into (20) and retaining the first-order terms yields:

$$\boldsymbol{R} \simeq \begin{bmatrix} \cos(\Omega_y) & -\sin(\Omega_y) & \sin(\Omega_y)\cdot\Omega_r(\phi) + \cos(\Omega_y)\cdot\Omega_p(\phi) \\ \sin(\Omega_y) & \cos(\Omega_y) & -\cos(\Omega_y)\cdot\Omega_r(\phi) + \sin(\Omega_y)\cdot\Omega_p(\phi) \\ -\Omega_p(\phi) & \Omega_r(\phi) & 1 \end{bmatrix}, \tag{A1}$$

where Ω_x, $x = r, p, y$ is the tilt angle already defined in Equation (19). r, p, y is shorthand notation for "roll", "pitch", and "yaw".

Appendix A.2. Wind-Vector Projection over the Rotated LiDAR Pointing Vector $\hat{r}_{rot}(\phi)$

In rotational motion, the FDWL-measured wind as a function of the scan phase, $f_{rot}(\phi)$, is the projection of the wind vector $\vec{u}$ on the LiDAR pointing vector $\hat{r}_{rot}(\phi)$. Inserting Equations (12) and (A1) into Equation (22) gives $\hat{r}_{rot}(\phi)$, and substituting this vector and definitional Equation (1) for the wind vector into Equation (23) gives the VAD function for the measured wind. The result can be expressed as follows:

$$\begin{aligned} f_{rot}(\phi) = \vec{u} \cdot \hat{r}_{rot}(\phi) = HWS \cdot [\cos(WD) \cdot (\sin(\theta_0) \cdot [\cos(\phi - \phi_0) \cdot r_{11} + \sin(\phi - \phi_0) \cdot r_{12}] \\ - \cos(\theta_0) \cdot r_{13}) + \sin(WD) \cdot (\sin(\theta_0) \cdot [\cos(\phi - \phi_0) \cdot r_{21} + \sin(\phi - \phi_0) \cdot r_{22}] \\ - \cos(\theta_0) \cdot r_{23})] + VWS \cdot (\sin(\theta_0) \cdot [\cos(\phi - \phi_0) \cdot r_{31} + \sin(\phi - \phi_0) \cdot r_{32}] \\ - \cos(\theta_0) \cdot r_{33}), \end{aligned} \tag{A2}$$

where coefficients $r_{ij}, i, j = 1 \ldots 3$ are the entries in the i-th row and j-th column of the rotation matrix $\boldsymbol{R}$ (Equation (A1)).

Appendix A.3. Fourier Coefficients for the Rotational Motion Model

In the rotational motion of the FDWL (Section 3.5.1), the first-order Fourier coefficients a_1^{rot} and b_1^{rot} of Equation (24) that give the HWS rotational error are obtained in analytical form by inserting Equation (A2) above into definitional Equation (18). They take the following form:

$$\begin{aligned} a_1^{rot} = \frac{1}{\pi} \int_0^{2\pi} f_{rot}(\phi) \cos(\phi) d\phi = \frac{1}{\pi} HWS \cdot [\cos(WD) \cdot (\sin(\theta_0) \cdot [\cos(y) I_{11} \\ - \sin(y) I_{12}] - \cos(\theta_0) \cdot [A_r \sin(y) I_{1,r} + A_p \cos(y) I_{1,p}]) \\ + \sin(WD) \cdot (\sin(\theta_0) \cdot [\sin(y) I_{11} + \cos(y) I_{12}] \\ - \cos(\theta_0) \cdot [-A_r \cos(y) I_{1,r} + A_p \sin(y) I_{1,p}])], \end{aligned} \tag{A3}$$

and

$$\begin{aligned} b_1^{rot} = \frac{1}{\pi} \int_0^{2\pi} f_{rot}(\phi) \sin(\phi) d\phi = \frac{1}{\pi} HWS \cdot [\cos(WD) \cdot (\sin(\theta_0) \cdot [\cos(y) I_{21} \\ - \sin(y) I_{22}] - \cos(\theta_0) \cdot [A_r \sin(y) I_{2,r} + A_p \cos(y) I_{2,p}]) \\ + \sin(WD) \cdot (\sin(\theta_0) \cdot [\sin(y) I_{21} + \cos(y) I_{22}] \\ - \cos(\theta_0) \cdot [-A_r \cos(y) I_{2,r} + A_p \sin(y) I_{2,p}])], \end{aligned} \tag{A4}$$

where coefficients I_{mn} and $I_{m,x}$ with $m, n = 1, 2$ and $x = r, p$ are the auxiliary integrals of Table A1. The mnemonic subscript $m = 1$ ($m = 2$) refers to the Fourier coefficient a_1 (b_1), and as mentioned, subscripts r and p denote "roll" and "pitch", respectively.

Appendix A.4. Fourier Coefficients for the Translational-Motion Model

In the translational motion, the FDWL-measured wind as a function of the scan phase, $f_{trans}(\phi)$ (Equation (28)), is the projection of the apparent wind vector (Equation (27)) on the LiDAR pointing vector (Equation (12)). The first step towards computing the Fourier coefficients is, therefore, computation of the apparent wind by substituting translational-velocity vector Equation (26) and definitional Equation (1) for the wind vector into Equation (27). The second step is substituting Equation (27) for the measured wind and Equation (12) for the LiDAR pointing vector into Equation (28), which gives the VAD function for the measured wind, $f_{trans}(\phi)$.

Finally, the first-order Fourier coefficients a_1^{trans} and b_1^{trans} in Equation (29), giving the HWS translational error, are derived in analytical form by inserting Equation (28) into definitional Equation (18). This gives

$$\begin{aligned} a_1^{trans} = \frac{1}{\pi} \int_0^{2\pi} f_{trans}(\phi) \cos(\phi) d\phi = \frac{1}{\pi} \cdot (\sin(\theta_0) \cdot [HWS \cdot (\cos(WD) I_{11} \\ + \sin(WD) I_{12}) - A_{su} \cdot I_{11,su} - A_{sw} \cdot I_{12,sw}] \\ + A_h \cdot \cos(\theta_0) \cdot I_{1,h}), \end{aligned} \tag{A5}$$

and

$$b_1^{trans} = \frac{1}{\pi}\int_0^{2\pi} f_{trans}(\phi)\sin(\phi)d\phi = \frac{1}{\pi}\cdot(\sin(\theta_0)\cdot[HWS\cdot(\cos(WD)I_{21} + \sin(WD)I_{22}) - A_{su}\cdot I_{21,su} - A_{sw}\cdot I_{22,sw}] + A_h\cdot\cos(\theta_0)\cdot I_{2,h}), \tag{A6}$$

where coefficients I_{mn}, $I_{m,x}$, and $I_{mn,x}$ with $m, n = 1, 2$ and $x = su, sw, h$ are the auxiliary integrals of Table A1. As mentioned, the mnemonic subscript $m = 1$ ($m = 2$) refers to the Fourier coefficient a_1 (b_1). The subscripts su, sw, and h denote the "surge", "sway", and "heave", respectively.

Appendix A.5. Auxiliary Integrals

Table A1. Auxiliary integrals for computation of the rotational- and translational-motion Fourier coefficients given by Equations (A3)–(A6), respectively. *Note* that not all possible subscript combinations are simultaneously used.

Coef.	$g(\phi)$	$\int_0^{2\pi} g(\phi)\, d\phi$
I_{11}	$\cos(\phi)\cdot\cos(\phi-\phi_0)$	$\pi\cdot\cos(\phi_0)$
I_{12}	$\cos(\phi)\cdot\sin(\phi-\phi_0)$	$-\pi\cdot\sin(\phi_0)$
I_{21}	$\sin(\phi)\cdot\cos(\phi-\phi_0)$	$\pi\cdot\sin(\phi_0)$
I_{22}	$\sin(\phi)\cdot\sin(\phi-\phi_0)$	$\pi\cdot\cos(\phi_0)$
$I_{1,x}$	$\cos(\phi)\cdot\sin(f_x\phi-\alpha_x)$	$-\frac{f_x}{f_x^2-1}\cdot[\cos(\alpha_x-2\pi f_x)-\cos(\alpha_x)]$ if $f_x=1\longrightarrow-\pi\sin(\alpha_x)$
$I_{2,x}$	$\sin(\phi)\cdot\sin(f_x\phi-\alpha_x)$	$-\frac{1}{f_x^2-1}\cdot[\sin(\alpha_x-2\pi f_x)-\sin(\alpha_x)]$ if $f_x=1\longrightarrow\pi\cos(\alpha_x)$
$I_{11,x}$	$\cos(\phi)\cdot\cos(\phi-\phi_0)\cdot\sin(f_x\phi-\alpha_x)$	$\frac{1}{f_x(f_x^2-4)}[f_x\sin(\phi_0)A_x-(f_x^2-2)\cos(\phi_0)B_x]$ if $f_x=2\longrightarrow\frac{\pi}{2}\sin(\alpha_x-\phi_0)$
$I_{12,x}$	$\cos(\phi)\cdot\sin(\phi-\phi_0)\cdot\sin(f_x\phi-\alpha_x)$	$\frac{1}{f_x(f_x^2-4)}[f_x\cos(\phi_0)A_x+(f_x^2-2)\sin(\phi_0)B_x]$ if $f_x=2\longrightarrow\frac{\pi}{2}\cos(\alpha_x-\phi_0)$
$I_{21,x}$	$\sin(\phi)\cdot\cos(\phi-\phi_0)\cdot\sin(f_x\phi-\alpha_x)$	$\frac{1}{f_x(f_x^2-4)}[f_x\cos(\phi_0)A_x+2\sin(\phi_0)B_x]$ if $f_x=2\longrightarrow\frac{\pi}{2}\cos(\alpha_x-\phi_0)$
$I_{22,x}$	$\sin(\phi)\cdot\sin(\phi-\phi_0)\cdot\sin(f_x\phi-\alpha_x)$	$\frac{1}{f_x(f_x^2-4)}[-f_x\sin(\phi_0)A_x+2\cos(\phi_0)B_x]$ if $f_x=2\longrightarrow\frac{\pi}{2}\sin(\alpha_x-\phi_0)$
	where: $x\in[r=roll, p=pitch$ $su=surge, sw=sway, h=heave]$	being: $A_x=\sin(\alpha_x)(1-\cos(2\pi f_x))+\cos(\alpha_x)\sin(2\pi f_x)$ $B_x=\sin(\alpha_x)\sin(2\pi f_x)-\cos(\alpha_x)(1-\cos(2\pi f_x))$

References

1. Global Wind Energy Council. *Global Wind Report 2018*; Technical Report; Global Wind Energy Council: Brussels, Belgium, 2019.
2. Barthelmie, R.; Courtney, M.; Højstrup, J.; Larsen, S. Meteorological aspects of offshore wind energy: Observations from the Vindeby wind farm. *J. Wind. Eng. Ind. Aerodyn.* **1996**, *62*, 191–211. [CrossRef]
3. Ramírez, L.; Fraile, D.; Brindley, G. *Offshore Wind in Europe Key Trends and Statistics 2019*; Technical Report; WindEurope: Brussels, Belgium, 2020.

4. Global Wind Energy Council. *Global Wind Report 2021*; Technical Report; Global Wind Energy Council: Brussels, Belgium, 2021.
5. Kost, K.; Mayer, J.N.; Thomsen, J.; Hartmann, N.; Senkpiel, C.; Philipps, S.; Nold, S.; Lude, S.; Saad, N.; Schlegl, T. *Levelized Cost of Electricity Renewable Energy Technologies*; Technical Report; Fraunhofer Institut for Solar Energy Systems (ISE): Freiburg, Germany, 2013.
6. Timmons, D. 25—Optimal Renewable Energy Systems: Minimizing the Cost of Intermittent Sources and Energy Storage. In *A Comprehensive Guide to Solar Energy Systems*; Letcher, T.M., Fthenakis, V.M., Eds.; Academic Press: Cambridge, MA, USA, 2018; pp. 485–504. . [CrossRef]
7. Carbon Trust. *Carbon Trust Offshore Wind Accelerator Roadmap for the Commercial Acceptance of Floating LiDAR Technology*; Technical Report; Carbon Trust: London, UK, 2018.
8. Roland Berger. *Offshore Wind toward 2020: On the Pathway to Cost Competitiveness*; Technical Report; Roland Berger: Munich, Germany, 2013.
9. Barthelmie, R.; Pryor, S. Can Satellite Sampling of Offshore Wind Speeds Realistically Represent Wind Speed Distributions? *J. Appl. Meteorol.* **2003**, *42*, 83–94. [CrossRef]
10. Chang, R.; Zhu, R.; Badger, M.; Hasager, C.B.; Zhou, R.; Ye, D.; Zhang, X. Applicability of Synthetic Aperture Radar wind retrievals on offshore wind resources assessment in Hangzhou Bay, China. *Energies* **2014**, *7*, 3339–3354. [CrossRef]
11. Hirth, B.D.; Schroeder, J.L.; Gunter, W.S.; Guynes, J.G. Measuring a utility-scale turbine wake using the TTUKa mobile research radars. *J. Atmos. Ocean. Technol.* **2012**, *29*, 765–771. [CrossRef]
12. Vogt, S.; Thomas, P. SODAR—A useful remote sounder to measure wind and turbulence. *J. Wind. Eng. Ind. Aerodyn.* **1995**, *54*, 163–172. [CrossRef]
13. Lang, S.; McKeogh, E. LIDAR and SODAR Measurements of Wind Speed and Direction in Upland Terrain for Wind Energy Purposes. *Remote Sens.* **2011**, *3*, 1871–1901. [CrossRef]
14. International Energy Association. *State of the art of Remote Wind Speed Sensing Techniques Using Sodar, Lidar and Satellites*; Technical Report; International Energy Association: Paris, France, 2007.
15. Sempreviva, A.M.; Barthelmie, R.J.; Pryor, S.C. Review of Methodologies for Offshore Wind Resource Assessment in European Seas. *Surv. Geophys.* **2008**, *29*, 471–497. [CrossRef]
16. Slinger, C.; Harris, M. *Introduction to Continuous-Wave Doppler Lidar*; Summer School in Remote Sensing for Wind Energy: Boulder, CO, USA, 2012.
17. Lolli, S.; Delaval, A.; Loth, C.; Garnier, A.; Flamant, P.H. 0.355-micrometer direct detection wind lidar under testing during a field campaign in consideration of ESA's ADM-Aeolus mission. *Atmos. Meas. Tech.* **2013**, *6*, 3349–3358. [CrossRef]
18. Reitebuch, O.; Werner, C.; Leike, I.; Delville, P.; Flamant, P.H.; Cress, A.; Engelbart, D. Experimental Validation of Wind Profiling Performed by the Airborne 10-µm Heterodyne Doppler Lidar WIND. *J. Atmos. Ocean. Technol.* **2001**, *18*, 1331–1344. [CrossRef]
19. Schuon, F.; González, D.; Rocadenbosch, F.; Bischoff, O.; Jané, R. KIC InnoEnergy Project Neptune: Development of a Floating LiDAR Buoy for Wind, Wave and Current Measurements. In Proceedings of the DEWEK 2012 German Wind Energy Conference, Bremen, Germany, 7–8 November 2012.
20. Silva, M.P.A.d.; Rocadenbosch, F.; Farré-Guarné, J.; Salcedo-Bosch, A.; González-Marco, D.; Peña, A. Assessing Obukhov Length and Friction Velocity from Floating Lidar Observations: A Data Screening and Sensitivity Computation Approach. *Remote Sens.* **2022**, *14*, 1394. [CrossRef]
21. Pichugina, Y.; Banta, R.; Brewer, W.; Sandberg, S.; Hardesty, R. Doppler Lidar–Based Wind-Profile Measurement System for Offshore Wind-Energy and Other Marine Boundary Layer Applications. *J. Appl. Meteorol. Climatol.* **2012**, *51*, 327–349. [CrossRef]
22. Gottschall, J.; Wolken-Möhlmann, G.; Lange, B. About offshore resource assessment with floating lidars with special respect to turbulence and extreme events. *J. Phys. Conf. Ser.* **2014**, *555*, 12–43. [CrossRef]
23. Salcedo-Bosch, A.; Rocadenbosch, F.; Gutiérrez-Antuñano, M.A.; Tiana-Alsina, J. Estimation of Wave Period from Pitch and Roll of a Lidar Buoy. *Sensors* **2021**, *21*, 1310. [CrossRef] [PubMed]
24. Salcedo-Bosch, A.; Gutierrez-Antunano, M.A.; Tiana-Alsina, J.; Rocadenbosch, F. Motional Behavior Estimation Using Simple Spectral Estimation: Application to the Off-Shore Wind Lidar. In Proceedings of the 2020 IEEE International Geoscience and Remote Sensing Symposium (IGARSS-2020), Waikoloa, HI, USA, 26 September–2 October 2020.
25. Gutiérrez-Antuñano, M.; Tiana-Alsina, J.; Salcedo, A.; Rocadenbosch, F. Estimation of the Motion-Induced Horizontal-Wind-Speed Standard Deviation in an Offshore Doppler Lidar. *Remote Sens.* **2018**, *10*, 2037. [CrossRef]
26. Salcedo-Bosch, A.; Gutierrez-Antunano, M.A.; Tiana-Alsina, J.; Rocadenbosch, F. Floating Doppler Wind Lidar Measurement of Wind Turbulence: A Cluster Analysis. In Proceedings of the 2020 IEEE International Geoscience and Remote Sensing Symposium (IGARSS-2020), Waikoloa, HI, USA, 26 September–2 October 2020.
27. Gutiérrez-Antuñano, M.A.; Tiana-Alsina, J.; Rocadenbosch, F. Performance evaluation of a floating lidar buoy in nearshore conditions. *Wind. Energy* **2017**, *20*, 1711–1726. [CrossRef]
28. Kelberlau, F.; Neshaug, V.; Lønseth, L.; Bracchi, T.; Mann, J. Taking the Motion out of Floating Lidar: Turbulence Intensity Estimates with a Continuous-Wave Wind Lidar. *Remote Sens.* **2020**, *12*, 898. [CrossRef]
29. Gottschall, J.; Gribben, B.; Stein, D.; Würth, I. Floating lidar as an advanced offshore wind speed measurement technique: Current technology status and gap analysis in regard to full maturity. *Wiley Interdiscip. Rev. Energy Environ.* **2017**, *6*, e250. [CrossRef]
30. Mücke, T.; Kleinhans, D.; Peinke, J. Atmospheric turbulence and its influence on the alternating loads on wind turbines. *Wind Energy* **2011**, *14*, 301–316. [CrossRef]

31. Désert, T.; Knapp, G.; Aubrun, S. Quantification and Correction of Wave-Induced Turbulence Intensity Bias for a Floating LIDAR System. *Remote Sens.* **2021**, *13*, 2973. [CrossRef]
32. Gottschall, J.; Wolken-Möhlmann, G.; Viergutz, T.; Lange, B. Results and conclusions of a floating-lidar offshore test. *Energy Procedia* **2014**, *53*, 156–161. [CrossRef]
33. Salcedo-Bosch, A.; Rocadenbosch, F.; Sospedra, J. A Robust Adaptive Unscented Kalman Filter for Floating Doppler Wind-LiDAR Motion Correction. *Remote Sens.* **2021**, *13*, 4167. [CrossRef]
34. Salcedo-Bosch, A.; Rocadenbosch, F.; Sospedra, J. Enhanced Dual Filter for Floating Wind Lidar Motion Correction: The Impact of Wind and Initial Scan Phase Models. *Remote Sens.* **2022**, *14*, 4704. [CrossRef]
35. Tiana-Alsina, J.; Gutiérrez, M.A.; Würth, I.; Puigdefàbregas, J.; Rocadenbosch, F. Motion compensation study for a floating doppler wind lidar. In Proceedings of the Geoscience and Remote Sensing Symposium Proceedings, Milan, Italy, 26–31 July 2015.
36. Bischoff, O.; Yu, W.; Gottschall, J.; Cheng, P.W. Validating a simulation environment for floating lidar systems. *J. Phys. Conf. Ser.* **2018**, *1037*, 052036. [CrossRef]
37. Salcedo-Bosch, A.; Farré-Guarné, J.; Sala-Álvarez, J.; Villares-Piera, J.; Rocadenbosch, F.; Tanamachi, R.L. Floating Doppler wind lidar simulator for horizontal wind speed measurement error assessment. In Proceedings of the 2021 IEEE International Geoscience and Remote Sensing Symposium (IGARSS-2021), Brussels, Belgium, 11–16 July 2021.
38. Kelberlau, F.; Mann, J. Quantification of Motion-Induced Measurement Error on Floating Lidar Systems. *Atmos. Meas. Tech. Discuss.* **2022**, *2022*, 1–31. [CrossRef]
39. Sospedra, J.; Cateura, J.; Puigdefàbregas, J. Novel multipurpose buoy for offshore wind profile measurements EOLOS platform faces validation at ijmuiden offshore metmast. *Sea Technol.* **2015**, *56*, 25–28.
40. Scientific, C. *ZephIR 300*; Technical Report; Campbell Scientific: Edmonton, AB, Canada, 2016.
41. Pitter, M.; Burin des Roziers, E.; Medley, J.; Mangat, M.; Slinger, C.; Harris, M. *Performance Stability of Zephir in High Motion Enviroments: Floating and Turbine Mounted*; Technical Report; ZephIR: Ledbury, UK, 2014.
42. Knoop, S.; Bosveld, F.C.; de Haij, M.J.; Apituley, A. A 2-year intercomparison of continuous-wave focusing wind lidar and tall mast wind measurements at Cabauw. *Atmos. Meas. Tech.* **2021**, *14*, 2219–2235. [CrossRef]
43. Gutiérrez Antuñano, M. Doppler Wind LIDAR Systems Data Processing and Applications: An Overview towards Developing the New Generation of Wind Remote-Sensing Sensors for Off-Shore Wind Farms. Ph.D. Thesis, Universitat Politècnica de Catalunya: Barcelona, Spain, 2019.
44. KIC InnoEnnergy. *Neptune Project Leaflet*; Technical Report; KIC InnoEnergy: Eindhoven, The Netherlands, 2015.
45. MicroStrain. *3DM-GX3® -45 Theory of Operation*; Technical Report; 459 Hurricane Lane: Williston, VT, USA, 2012.
46. Barlow, R.J. *Statistics: A Guide to the Use of Statistical Methods in the Physical Sciences*; Manchester Physics Series; Wiley: Chichester, UK, 1989.
47. Pênha, A.; Hasager, C.; Merete, B.; Barthelmie, R.; Ferhat, B.; Jean-Pierre, C.; Stefan, E.; Frandsen, S.; Michael, H.; Ioanna, K.; et al. *Remote Sensing for Wind Energy*; DTU Wind Energy: Roskilde, Denmark, 2015.
48. Tolstov, J. P. *Fourier Series*; Prentice-Hall Inc.: Englewood Cliffs, N.J., USA, 1962.
49. Stearns, S.D.; Hush, D.R. *Digital Signal Processing with Examples in MATLAB*, 2nd ed.; Taylor & Francis Inc.: Bosa Roca, FL, USA, 2011.
50. Stade, E. *Fourier Analysis*, 1st ed.; Wiley-Interscience: Hoboken, NJ, USA, 2015.
51. Kogaki, T.; Sakurai, K.; Shimada, S.; Kawabata, H.; Otake, Y.; Kondo, K.; Fujita, E Field Measurements of Wind Characteristics Using LiDAR on a Wind Farm with Downwind Turbines Installed in a Complex Terrain Region. *Energies* **2020**, *13*, 5135. [CrossRef]
52. Palais, B.; Palais, R.; Rodi, S. A Disorienting Look at Euler's Theorem on the Axis of a Rotation. *Am. Math. Mon.* **2009**, *116*, 892–909. [CrossRef]
53. Roithmayr, C.M.; Hodges, D.H. *Dynamics: Theory and Application of Kane's Method*; American Society of Mechanical Engineers Digital Collection; NASA-Langley Research Center: Hampton, VA, USA, 2016.
54. Proakis, J.; Manolakis, D. *Digital Signal Processing*, 4th ed.; Prentice Hall: Upper Saddle River, NJ, USA, 2006.
55. Plancherel, M.; Leffler, M. Contribution À L'Étude de la reprÉsentation D'une fonction arbitraire par des intÉgrales dÉfinies. *Rend. Del Circ. Mat. Palermo (1884–1940)* **1910**, *30*, 289–335. [CrossRef]
56. Yao, G.; Xie, J.; Huang, W. HF Radar Ocean Surface Cross Section for the Case of Floating Platform Incorporating a Six-DOF Oscillation Motion Model. *IEEE J. Ocean. Eng.* **2021**, *46*, 156–171. [CrossRef]
57. Wan, B.; Wu, X.; Yue, X.; Zhang, L.; Wang, L. Calibration of Phased-Array High-Frequency Radar on an Anchored Floating Platform. *Remote Sens.* **2022**, *14*, 2174. [CrossRef]
58. Wagner, R.; Mikkelsen, T.; Courtney, M. *Investigation of Turbulence Measurements with a Continuous Wave, Conically Scanning LiDAR*; Technical Report; DTU: Roskilde, Denmark, 2009.
59. Gottschall, J.; Courtney, M.S.; Wagner, R.; Jørgensen, H.E.; Antoniou, I. Lidar profilers in the context of wind energy–a verification procedure for traceable measurements. *Wind Energy* **2012**, *15*, 147–159. [CrossRef]
60. Jeffreys, H.; Taylor, G.I. On the formation of water waves by wind. *Proc. R. Soc. Lond. Ser. A Contain. Pap. Math. Phys. Character* **1925**, *107*, 189–206. [CrossRef]

61. IEA Wind TCP. Available online: https://iea-wind.org/ (accessed on 3 March 2023).
62. Task 52—Large-Scale Deployment of Wind Lidar | IEA Wind TCP. Available online: https://iea-wind.org/task52/ (accessed on 3 March 2023).